

Efficiency of charge transfer in changing the dissociation dynamics of OD^+ transients formed after the photo-fragmentation of D_2O

Cite as: J. Chem. Phys. 159, 000000 (2023); doi: 10.1063/5.0159300

Submitted: 22 May 2023 • Accepted: 7 August 2023 •

Published Online: 9 99 9999



W. Iskandar,¹ T. N. Rescigno,¹ A. E. Orel,² T. Severt,³ K. A. Larsen,^{1,4} Z. L. Streeter,^{1,5} B. Jochim,³ B. Griffin,^{1,6} D. Call,⁶ V. Davis,⁶ C. W. McCurdy,^{1,5} R. R. Lucchese,¹ J. B. Williams,⁶ I. Ben-Itzhak,³ D. S. Slaughter,¹ and Th. Weber^{1,a)}

AFFILIATIONS

¹Chemical Sciences Division, Lawrence Berkeley National Laboratory, Berkeley, California 94720, USA

²Chemical Engineering, University of California, Davis, California 95616, USA

³J.R. Macdonald Laboratory, Department of Physics, Kansas State University, Manhattan, Kansas 66506, USA

⁴Graduate Group in Applied Science and Technology, University of California, Berkeley, California 94720, USA

⁵Department of Chemistry, University of California, Davis, California 95616, USA

⁶Department of Physics, University of Nevada, Reno, Nevada 89557, USA

^{a)}Author to whom correspondence should be addressed: tweber@lbl.gov

ABSTRACT

We present an investigation of the relaxation dynamics of deuterated water molecules after direct photo-double ionization at 61 eV. We focus on the very rare $\text{D}^+ + \text{O}^+ + \text{D}$ reaction channel in which the sequential fragmentation mechanisms were found to dominate the dynamics. Aided by theory, the state-selective formation and breakup of the transient OD^+ ($a^1\Delta$, $b^1\Sigma^+$) is traced, and the most likely dissociation path— $\text{OD}^+ : a^1\Delta$ or $b^1\Sigma^+ \rightarrow A^3\Pi \rightarrow X^3\Sigma^- \rightarrow B^3\Sigma^-$ —involving a combination of spin-orbit and non-adiabatic charge transfer transitions is determined. The multi-step transition probability of this complex transition sequence in the intermediate fragment ion is directly evaluated as a function of the energy of the transient OD^+ above its lowest dissociation limit from the measured ratio of the $\text{D}^+ + \text{O}^+ + \text{D}$ and competing $\text{D}^+ + \text{D}^+ + \text{O}$ sequential fragmentation channels, which are measured simultaneously. Our coupled-channel time-dependent dynamics calculations reproduce the general trends of these multi-state relative transition rates toward the three-body fragmentation channels.

Published under an exclusive license by AIP Publishing. <https://doi.org/10.1063/5.0159300>

I. INTRODUCTION

The concept of reaction coordinates is elemental in chemistry as it describes the evolution from reactants to products with various intermediates and transition states in between. Transition states and their reaction rates are nearly impossible to observe and identify, as their activation energies, i.e., the local maxima on the potential energy landscape, cannot be directly measured. However, it is not only the activation energy that is crucial to the progress of bond-forming and bond-breaking reaction steps. Charge redistribution and electron transfer during a chemical reaction also influence the possible pathways and outcomes, as well as the reaction rates. Among several processes, electron transfer in single molecules can

be initiated by spin-orbit coupling (SOC), which is a relativistic quantum effect due to the coupling of the electronic orbital angular momentum and spin. SOC happens between electronic states having potential surfaces that cross, approach each other, or run parallel in any nuclear degree of freedom.¹ The relevant geometries for these conditions may be far from equilibrium and represent a small subset of the accessible potential energy surfaces. Therefore, in many molecules consisting of light atoms, the role of SOC is considered to be rather minimal.²

It is at the heart of modern ultrafast science to trace and time the coupled non-adiabatic motion of electrons and nuclei in molecular dissociation processes that create transitional species, which make effective SOC possible and consequently impact the

mechanisms and outcomes of chemical reactions. In this study, we follow the creation of a short-lived molecular ion intermediate in either of two different electronic states. Moreover, we measure the transition probabilities of OD^+ leading to $\text{O}^+ + \text{D}$ or $\text{D}^+ + \text{O}$ dissociation, which are multi-step transitions governed by SOC and charge transfer.

The double ionization of (deuterated) water followed by the breakup of the dication is an ideal system in which to study such dynamics. It can lead to many fragmentation channels depending on the populated electronic state as well as on the rotational and vibrational modes of the molecule. The water dication can fragment into two bodies, $\text{D}^+ + \text{OD}^{+3-14}$ and $\text{D}_2^+ + \text{O}^+$,^{5,6,15-19} or dissociate into the competing three-body channels $\text{D}^+ + \text{D}^+ + \text{O}$ ^{7,12,14,20,21} and $\text{D}^+ + \text{O}^+ + \text{D}$.^{3-12,22-24} The latter, $\text{D}^+ + \text{O}^+ + \text{D}$, fragmentation channel is especially interesting as it is very rare compared to the $\text{D}^+ + \text{D}^+ + \text{O}$ breakup, even though the dissociation limits of these two channels are nearly degenerate. Production of the D^+ and O^+ fragments may happen directly following double ionization or proceed in a sequential way, i.e., by breaking one bond at a time, depending on the photon energy and the reaction pathway on the multi-dimensional potential energy surfaces (PESs). PESs and non-adiabatic coupling matrix elements, even for simple triatomic molecules, are not widely available for highly excited and dication states, as they are expensive to calculate, and, hence, the interpretation of the experimental results is challenging. We hasten to add that, for small molecules, alternative theoretical approaches are feasible.²⁵

In contrast to the rare $\text{D}^+ + \text{O}^+ + \text{D}$ channel, the direct and sequential (also known as concerted and stepwise, respectively) photodissociation of D_2O^{2+} into $\text{D}^+ + \text{D}^+ + \text{O}$ has been studied in great differential detail in a collaboration of experiment and theory.^{14,20,21} There have also been a number of earlier investigations in which the $\text{D}^+ + \text{O}^+ + \text{D}$ fragmentation channels have been observed. These studies included ion impact,^{7,8,22} electron impact,^{9-12,23} and single-photon double ionization.^{3-6,24} Yet none of these studies followed the dynamics of the transient reaction products. Instead, these experiments focused on identifying the fragmentation channels with, in some cases, speculations about the electronic states involved. They found contributions from either direct dissociation, indirect double ionization, or fragmentation via multi-step processes. Most of these studies obtained wide distributions of kinetic energy release (KER) upon fragmentation, covering energies from 5 eV up to 50 eV, which can be explained by the population of a variety of excited states of the dissociating D_2O^{2+} dication that eventually results in the final products mentioned above. Photoabsorption experiments close to the double ionization threshold^{3,4} yielded KER distributions centered at about 5 eV, which are considerably smaller than the KER values obtained in the x-ray regime^{5,6} or in electron-^{11,12} and ion-impact studies⁸ where Auger decay is the dominant process. The smaller KER studies must involve autoionization or a sequential dissociation process since the potential energy curves (PECs, i.e., cuts through the PESs, depicted in Fig. 2 of Ref. 20) of the states leading directly to $\text{D}^+ + \text{O}^+ + \text{D}$ fragmentation after double ionization of D_2O lie some 20 eV above the vertical double ionization threshold and are steeply repulsive. To maintain the present focus on pathways involving SOC in the molecular transient, we will not discuss autoionization further in this work and refer the reader to a separate publication by the authors for that study.²⁶

Despite all these investigations on the three-body fragmentation of D_2O into $\text{D}^+ + \text{O}^+ + \text{D}$, a complete picture of the sequential fragmentation processes at play in water after photo-double ionization (PDI) is still lacking. The evolution of intermediate species remains elusive because their transition rates cannot be easily identified and followed in the lab. In this report, the formation and dissociation of the transient OD^+ in its excited electronic states are observed, and the branching ratios (BR) for the production of two competing three-body channels, $\text{D}^+ + \text{D}^+ + \text{O}$ and $\text{D}^+ + \text{O}^+ + \text{D}$, are measured simultaneously and quantified by theory. Importantly, as we will see below, this branching ratio is the direct measure of the $\text{A } ^3\Pi \rightarrow \text{X } ^3\Sigma^- \rightarrow \text{B } ^3\Sigma^-$ transition probability in the dissociating OD^+ intermediate.

II. EXPERIMENT

The experiments were performed at the undulator beamline 10.0.1.3 at the Advanced Light Source (ALS) synchrotron ring at Lawrence Berkeley National Laboratory (LBNL) using 61.0 eV linearly polarized photons to investigate the fragmentation dynamics of D_2O molecular targets. The photon energy resolution was set to ~ 200 meV using the 10.0.1 monochromator.²⁷ Since the fragmentation channel of interest is very rare, the photon energy of 61.0 eV was chosen to be near the maximum of the PDI cross section of the water molecule. The experimental setup was similar to the one described in Ref. 14. In brief, a preheated supersonic gas jet consisting of D_2O vapor with a stagnation pressure of 2 bar was formed by heating the nozzle, the gas line, and the D_2O reservoir to temperatures of 125, 115, and 105 °C, respectively. The supersonic gas jet was collimated laterally by two skimmers (with 0.3 and 0.5 mm orifice diameters) and then crossed with a photon beam inside the particle 3D-momentum imaging spectrometer of a reaction microscope, a.k.a. the COLd Target Recoil Ion Momentum Spectroscopy (COLTRIMS) apparatus.²⁸⁻³⁰ A static electric field of 12.2 V/cm and a parallel magnetic field of 10.2 G guided electrons and ions to two micro-channel plate detectors, each equipped with a delay line readout,^{31,32} which were located at the opposite ends of the spectrometer. Electrons of up to 30 eV and ionic fragments of up to 22 eV were collected with 4π solid angle. The neutral O and neutral D fragments of the competing $\text{D}^+ + \text{D}^+ + \text{O}$ and $\text{D}^+ + \text{O}^+ + \text{D}$ reaction channels were not measured directly, but their momenta were derived using momentum conservation. Choosing D_2O as the target molecule enabled us to distinguish between PDI events from any residual H_2O background present in the vacuum chamber ($\approx 1.2 \times 10^{-8}$ Torr) and the supersonic gas jet. Moreover, the electric extraction field and spectrometer geometry were optimized to ensure that there was no overlap between the $\text{D}^+ + \text{O}^+ + \text{D}$ channel and the neighboring $\text{OH}^+ + \text{D}$ and $\text{OD}^+ + \text{D}^+$ two-body breakups in the PhotoIonPhotoIon COincidence (PIPICO) time-of-flight (TOF) spectrum (not shown here). Hence, the breakup channel of interest could be cleanly isolated in the PIPICO-TOF for further analysis.

Photoionization above the double ionization threshold leads to the dissociation of D_2O^{2+} , primarily to $\text{D}^+ + \text{D}^+ + \text{O}$ or $\text{D}^+ + \text{OD}^+$ (see Ref. 14 for the iso-energetic H_2O molecule). The $\text{D}^+ + \text{O}^+ + \text{D}$ three-body breakup channel is very weak. Nevertheless, in the present study, it could be identified and isolated with significant statistics for detailed analysis. The PDI yield branching

168 ratios of these three fragmentation channels are 47.5% for $\text{OD}^+ +$
169 D^+ , 51.8% for $\text{D}^+ + \text{D}^+ + \text{O}$, and 0.7% for $\text{D}^+ + \text{O}^+ + \text{D}$ with a
170 *relative* error of $\leq 1\%$ each. The 47.5% for $\text{D}^+ + \text{OD}^+$ refers to the
171 fraction that goes into long-lived rovibrational states of OD^+ (hav-
172 ing lifetimes longer than the $4 \mu\text{s}$ TOF to the detector) and does not
173 contribute to what is observed as three-body dissociation, while the
174 51.8% refers to the total fraction that fragments into $\text{D}^+ + \text{D}^+ + \text{O}$
175 either via direct or sequential breakup.

176 In general, the branching ratios are affected by the detection
177 efficiencies of the D^+ , O^+ , and OD^+ ions on the MCP detector,
178 which scale with E/\sqrt{m} of the particles. Yet, with an overall kinetic
179 energy of around 2.2 keV gained in the particle extraction and
180 post-acceleration regions of the imaging spectrometer, the ion detec-
181 tion efficiencies of all species measured are actually very similar
182 (specifically, they are estimated to be ≈ 0.5 for O^+ and average to
183 the same value for particles like H_2^+ and D^+ according to Ref. 33.
184 Values for OD^+ are not known but are expected to be the same as
for O^+).

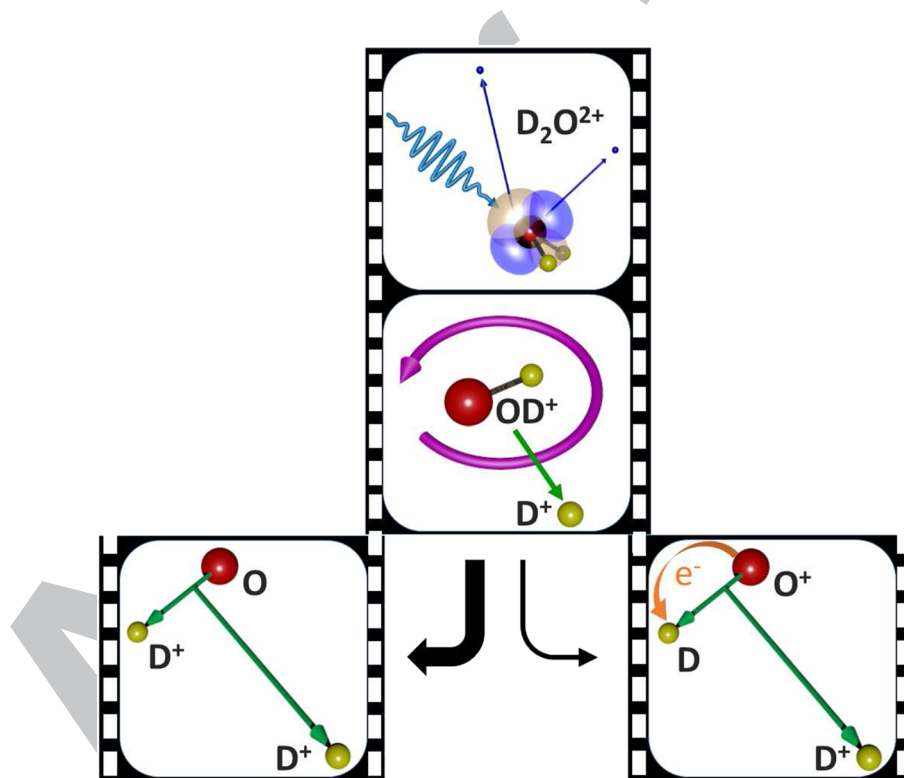
185 III. SEQUENTIAL BREAKUP OF D_2O^{2+} INTO $\text{D}^+ + \text{O}^+ + \text{D}$

186 As mentioned in the introduction, the rare $\text{D}^+ + \text{O}^+ + \text{D}$
187 three-body breakup channel is further characterized by the competi-
188 tion between direct double ionization and autoionization processes.

The investigation of the autoionization process can be found in
193 Ref. 26. In the present work, we isolate and analyze the direct
194 PDI process. We achieve this by selecting the PDI events in which
195 either of the two detected electrons exhibits a kinetic energy of
196 $E_e \geq 2.5 \text{ eV}$, which primarily excludes low energy electrons that typ-
197 ically stem from double ionization involving auto-ionization (see
198 Fig. 9 in Appendix A). In the next steps, we determine the relevant
199 water dication states and fragmentation mechanisms at play, iden-
200 tify the sequential fragmentation events of interest (see Sec. III A),
201 and then trace the dissociation pathways governed by SOC and
202 charge transfer that lead to the final products $\text{D}^+ + \text{O}^+ + \text{D}$ (see
203 Sec. III B). This enables us to retrieve the branching ratios for the
204 electronically excited OD^+ transients that dissociate to $\text{O}^+ + \text{D}$
205 (see Sec. III C).
206

207 A. Electronic states and fragmentation mechanisms

208 **Water Dication States:** Absorbing a 61 eV photon in water can
209 photo(double)ionize the target and populate several valence dication
210 states (see the top panel in Fig. 1). The measured electron sum
211 energy (see Fig. 10 in Appendix A) peaks around 17.2 eV and spans
212 the six lowest excited dication states, 1^1A_1 , 1^1B_1 , 1^3A_2 , 1^3B_2 , 2^1A_1 ,
213 and 1^1A_2 . None of these correlate with the $\text{D}^+ + \text{O}^+ + \text{D}$ dissoci-
214 ation limit directly. In the investigation reported here, we mainly



189 **FIG. 1.** Sketch of the PDI of D_2O populating several dication states (upper panel), followed by the two-body breakup into $\text{OD}^+ + \text{D}^+$, providing ample time for the transient
190 OD^+ ion to rotate (middle panel) before either dissociating into $\text{D}^+ + \text{D}^+ + \text{O}$ or, less likely, electron transfer in the OD^+ intermediate takes place, which is producing
191 $\text{D}^+ + \text{O}^+ + \text{D}$ (lower panel). Mainly the two water dication states 1^1B_1 and 2^1A_1 are populated, which feed the transient OD^+ ($a^1\Delta$, $b^1\Sigma^+$), respectively, in each fragmentation
192 channel. These sequential dissociation routes can be exquisitely followed with the native fame analysis (see text).
215
216
217
218

focus on the 1^1B_1 and 2^1A_1 states, as they are known for having substantial contributions from sequential fragmentation²¹ and, therefore, are promising candidates to study the formation and dissociation of OD^+ intermediates. While the 1^1A_1 dication state might be considered as well because it undergoes predominantly (98.4%)²⁰ two-body breakup, it feeds the bound electronic ground state of OD^+ with insufficient internal energy to dissociate and yield notable three-body production.¹³ While focusing on the 1^1B_1 and 2^1A_1 dications, at this point, we cannot dismiss the possibility that there are other competing states and dissociation mechanisms that contribute to the $D^+ + O^+(^4S) + D$ production with similar excess energy and KER.

To determine the dissociation limit of the $D^+ + O^+ + D$ three-body breakup channel of interest, we plot in Fig. 2 the measured yield distribution of the total kinetic energy of the final products, i.e., the measured sum energy of the two electrons and the KER. The presented spectrum reveals that the direct PDI (black line) leading to $D^+ + O^+ + D$ ends up at a dissociation limit very close to the $D^+ + D^+ + O(^3P)$ breakup (purple line). We thus conclude that the measured total kinetic energy is correlated with the $D^+ + O^+(^4S) + D$ limit, which is nearly degenerate with the $D^+ + D^+ + O(^3P)$ limit (with an energy gap of ≈ 20 meV)^{34,35} and is well below the next nearest dissociation limit of $D^+ + O^+(^2D) + D$, which is expected to be 3.3 eV higher.

Fragmentation Routes: The sequential fragmentation of D_2O^{2+} ($1^1B_1, 2^1A_1$) into $D^+ + D^+ + O(^3P)$ via $D^+ + OD^+$ has been recently investigated with a focus on two breakup paths.²¹ The second step in this sequential fragmentation process, namely the OD^+ dissociation to $D^+ + O(^3P)$, is driven by the SOC between the $a^1\Delta$ or $b^1\Sigma^+$ intermediate states and the $A^3\Pi$ state of OD^+ , the latter correlating with $O(^3P) + D^+$. We now seek to understand if additional SOC and charge transfer can alter the dissociation pathway leading to $D^+ + D^+ + O$ such that it can produce $D^+ + O^+ + D$. If sequential fragmentation into $D^+ + O^+ + D$ proceeds via the same transient OD^+ states, then a distinguishing mechanism must exist in the second breakup step, i.e., the OD^+ dissociation yielding $O^+(^4S) + D$

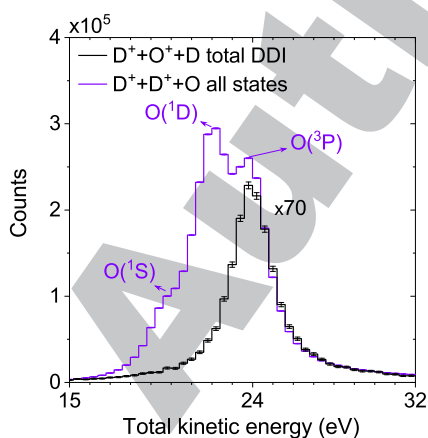


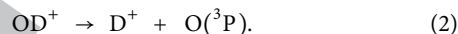
FIG. 2. Total kinetic energy $E_{sum} + KER$ for the $D^+ + D^+ + O$ breakup (purple line) and for the direct double ionization (DDI) process leading to $D^+ + O^+ + D$ (black line) upon PDI of D_2O with 61 eV photons. All error bars reflect one standard deviation of the statistical uncertainty.

instead of $D^+ + O(^3P)$. Next, we will track the OD^+ intermediate and quantify the ratio of each reaction channel produced during the dissociation process of this transient ion. This ratio is a direct measure of the transition probability leading to an OD^+ dissociation into $O^+ + D$ rather than $D^+ + O$.

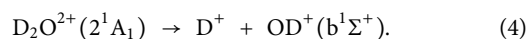
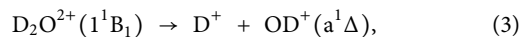
Sequential Dissociation: We now turn our attention to the investigation of the kinematics and energetics of this breakup process. Specifically, we are interested in the dynamics of the populated metastable states of the OD^+ intermediate, which were identified by Gervais *et al.*¹³ and examined in our recent joint experimental/theoretical study.²¹ Specifically, this sequential breakup in heavy water, observed in our experiment, begins with the two-body dissociation (see middle panel in Fig. 1),



followed by the dissociation of the metastable OD^+ transient ion (see bottom panel in Fig. 1),

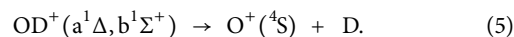


Between these two fragmentation steps, the intermediate excited OD^+ fragment rotates for a sufficient duration, i.e., longer than its rotational period (estimated to be about 1 ps using the rigid-rotor approximation for OD^+ at $R_{O-D} = 2$ a.u. and $j = 1$), in the fragmentation plane to erase any angular correlation between the two breakup steps, therefore leading to a uniform angular distribution of the $O-D^+$ dissociation direction [Eq. (2)] with respect to the OD^+-D^+ breakup axis of the first dissociation step [Eq. (1)]. We used this assumed full rotation of the OD^+ intermediate to extract the dynamics of this sequential fragmentation process and identified two specific pathways,²¹ namely



To reach the intermediate $D^+ + OD^+(a^1\Delta, b^1\Sigma^+)$ dissociation limit in this sequential breakup, the $D_2O^{2+}(1^1B_1, 2^1A_1)$ dication needs to undergo an asymmetric stretch starting from its symmetric C_{2v} geometry [for PECs, see Fig. 1(a) in Ref. 21]. We will be labeling the various water dication states by their symmetric (C_{2v}) spectroscopic designations, $A_1, A_2, B_1,$ and B_2 , with the understanding that at asymmetric geometries these should be replaced by their C_s designations, $A', A'', A''',$ and A'''' , respectively.

Both intermediate OD^+ states listed in Eqs. (3) and (4) can lead to the $D^+ + D^+ + O(^3P)$ final products via a spin-orbit mediated transition from the $a^1\Delta$ or $b^1\Sigma^+$ to the $A^3\Pi$ state of the metastable OD^+ fragment.^{13,36} However, it is also conceivable for a more exotic sequential process to occur, wherein the dissociating intermediate OD^+ molecule undergoes a different spin-orbit mediated transition, enabling dissociation to the $O^+ + D$ limit, namely



The latter fragmentation step listed in Eq. (5) results in the very rare three-body breakup $D^+ + O^+(^4S) + D$, which is the reaction channel of interest in this study (see bottom panel in Fig. 1).

To summarize, in this reaction, the 1^1B_1 and 2^1A_1 water dication states, which predominately dissociate in a sequential fashion to $D^+ + OD^+$, feed the electronically excited $a^1\Delta$ and $b^1\Sigma^+$ states of the OD^+ cation [see Eqs. (3) and (4)]. The PECs of the OD^+ ion and the vibrational levels of the $a^1\Delta$ and $b^1\Sigma^+$ states of the intermediate OD^+ ionic fragment, both correlating with the $D^+ + O(^1D)$ dissociation limit, are shown in Fig. 3.

We used the native frames analysis method^{21,37,38} to confirm these OD^+ cation states as active transients in our experiment, producing $D^+ + O^+ + D$ (see Appendix B for details about the method). The native frame analysis provides us with the emission angles and kinetic energies of the two separate dissociation steps and is thus well-suited for the following in-depth investigation of the sequential fragmentation. In Fig. 4, we plot all the measured $D^+ + O^+ + D$ events (except the ones associated with autoionization) as a function of the kinetic energy released in the second step, KER_{OD} , and the angle $\theta_{OD,D}$ between the conjugate momenta of the first dissociation step ($OD^+ - D^+$) and the second dissociation step ($O^+ - D$).

The broad angular distribution at low KER_{OD} , within the red rectangle in Fig. 4, resembles to some degree the distribution expected for a slow sequential breakup via an OD^+ intermediate, which rotates long enough in the fragmentation plane to yield a nearly uniform angular distribution, as expected in our native frames analysis. However, looking more closely, the projected angular distribution of the relevant events within the red rectangle in Fig. 4, shown in Fig. 5, is far from the expected flat distribution, $N(\theta_{OD,D}) = \text{constant}$, i.e., a uniform emission pattern in the fragmentation plane [compare with the uniform distribution in Fig. 2(c) in Ref. 21 for the $D^+ + D^+ + O$ channel and also see Fig. 11 in Appendix C]. Note that $\theta_{OD,D}$ is the angle between the conjugate momenta $P_{OD,D}$ and P_{OD} vectors, which define the fragmentation

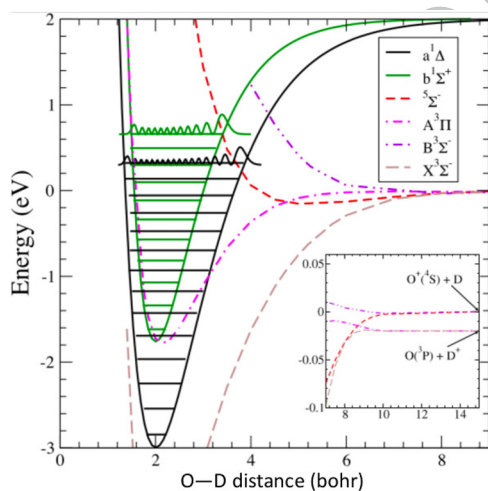


FIG. 3. Selected OD^+ PECs. The vibrational levels of the $a^1\Delta$, $b^1\Sigma^+$, and $1^1\Pi$ cation states are shown, as well as the PECs of the $5^3\Sigma^-$, $A^3\Pi$, $X^3\Sigma^-$, and $B^3\Sigma^-$ states. The dissociation limits of the latter four states are shown in the zoomed-in inset. The $a^1\Delta$, $b^1\Sigma^+$, and $1^1\Pi$ states all dissociate to $D^+ + O(^1D)$, 1.95 eV above the $O(^4S) + D$ dissociation limit. The zero of energy is taken to be the $O(^4S) + D$ dissociation limit.

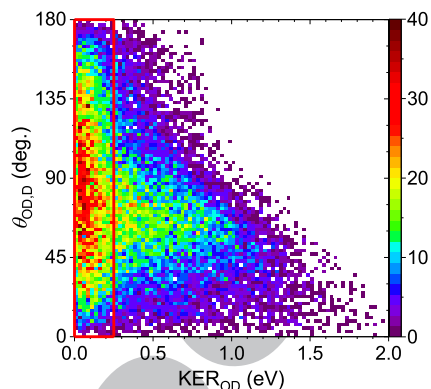


FIG. 4. All $D^+ + O^+ + D$ events of D_2O following direct PDI with 61 eV photons as a function of the kinetic energy release in the second breakup step, KER_{OD} , and the angle, $\theta_{OD,D}$, between the conjugate momenta of the first and second dissociation steps. The broad angular distribution at low KER_{OD} (i.e., within the red rectangle) is associated with the sequential breakup of D_2O^{2+} via the $D^+ + OD^+$ intermediate, followed by $OD^+ \rightarrow O^+ + D$ (i.e., resulting in the final products $D^+ + O^+ + D$). The events outside the red rectangle, which also yield $D^+ + O^+ + D$, stem from fragmentation Scenarios (1) and (3), described in this paper (see Appendix E), as well as from other dissociation mechanisms that will be discussed in detail elsewhere.

plane, and it represents the rotation of the second breakup direction relative to the first step within this plane (therefore, this angular distribution is plotted with equal bins in Figs. 4 and 5). This puzzling angular distribution is a consequence of the poor momentum resolution of the inferred neutral D fragment in our experiment and the very low KER_{OD} (≤ 0.25 eV) in the second step of this fragmentation process. In Fig. 5, we also show a simulated angular distribution that is expected once the experimental uncertainties

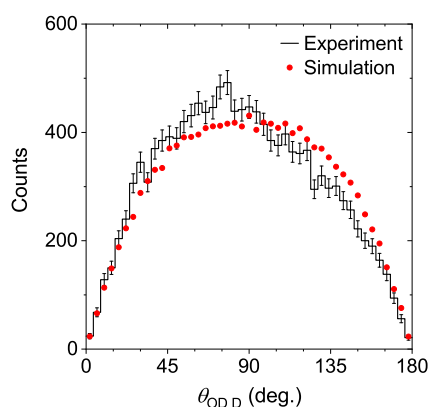


FIG. 5. Measured $D^+ + O^+ + D$ events with $KER_{OD} < 0.25$ eV upon PDI of D_2O with 61 eV photons as a function of the angle, $\theta_{OD,D}$, between the conjugate momenta of the first and second dissociation steps. The simulated data reflect the effect the experimental uncertainties have on this angular distribution for an assumed initial uniform distribution, i.e., $N(\theta_{OD,D}) = \text{constant}$ (see text and Appendix C). The degree of asymmetry of the distribution around its mean, i.e., the skewness, is 0.13 for the experimental distribution, while the simulated distribution is symmetric about 90° (i.e., skewness = 0). All error bars reflect one standard deviation of the statistical uncertainty.

affecting the expected uniform angular distribution are included (see Appendixes C and D for details). For the most part, this simulated distribution agrees with the measured one, therefore supporting the assignment of the events within the red rectangle in Fig. 4 as sequential fragmentation via an OD^+ intermediate, which rotates in the fragmentation plane and has a KER_{OD} smaller than 0.25 eV. However, there is a noticeable mismatch between the experimental and simulated distributions of $\theta_{\text{OD,D}}$. The experimental distribution of $\theta_{\text{OD,D}}$ is asymmetric (skewness = 0.13), while the simulated distribution is centered at 90° . This small mismatch indicates the presence of another dissociation scenario at play leaking in from fragmentation mechanisms that are mainly present outside the red rectangle in Fig. 4. As can be seen in Fig. 4, events outside the red rectangle show $\theta_{\text{OD,D}}$ peaking between 45° and 90° , which is in agreement with the direction of the observed skewness in Fig. 5.

Competing Minor Direct Fragmentation Scenario: Indeed, after careful examination, we also found that a direct three-body fragmentation into $\text{D}^+ + \text{O}^+ + \text{D}$, proceeding via symmetric OD stretch, is possible for direct PDI, populating the 1^1B_1 state [Scenario (1) in Appendix E 1]. It has similar energetics and kinematics in the lab frame and molecular frame as the sequential breakup and partly resides inside the red rectangle of Fig. 4 (see Appendix E 3 for details). The direct and sequential dissociation routes cannot be completely separated. This dissociation scenario, which is also present outside the red rectangle in Fig. 4, is part of the reason for the observed skewness in Fig. 5. Yet, the direct fragmentation involving SOC driven transitions from the 1^1B_1 state of D_2O^{2+} to either of the neighboring 2^3A_2 or 2^3B_2 triplet states, on which the water dication symmetrically stretches and finally reaches the $\text{D}^+ + \text{O}^+ + \text{D}$ dissociation limit, is a minor channel contributing 16% at most, compared to the sequential dissociation of this dication state; for completeness, the experimental and theoretical findings of this breakup scenario are described in Appendix E 3.

Other fragmentation routes via intermediates such as $\text{OD}^{2+} + \text{D}$ or $\text{D}_2^+ + \text{O}^+$ as the first dissociation step are not energetically accessible, as observed from the measured electron sum energy. Hence, we can conclude that the sequential fragmentation process via the OD^+ transient is mainly governed by the dissociation pathways of the 1^1B_1 or 2^1A_1 states of the water dication to produce $\text{D}^+ + \text{O}^+ + \text{D}$.

While we have identified a slow sequential breakup as the most prominent dissociation pathway for the events in the red rectangle in Fig. 4 ($\text{KER}_{\text{OD}} \leq 0.25$ eV), at this point we still cannot rule out the possibility that other states besides the two identified 1^1B_1 and 2^1A_1 dication states may contribute to these events.

B. Sequential dissociation pathways via $\text{D}^+ + \text{OD}^+$

Tracing the OD^+ Dissociation: In the following, we focus on the sequential fragmentation pathways of the D_2O^{2+} (1^1B_1 , 2^1A_1) dication leading to a three-body breakup. After establishing that both reaction channels—the dominant $\text{D}^+ + \text{D}^+ + \text{O}$ and the rare $\text{D}^+ + \text{O}^+ + \text{D}$ —start out via the same sequential $\text{D}^+ + \text{OD}^+$ dissociation pathway, we now have to understand how additional SOC or charge transfer transitions in OD^+ ($a^1\Delta$, $b^1\Sigma^+$) produce $\text{O}^+(^4\text{S}) + \text{D}$ instead of $\text{D}^+ + \text{O}(^3\text{P})$. Returning to Fig. 4, we note that sequential fragmentation via OD^+ yields a very low KER_{OD} in

the second step, i.e., the OD^+ dissociation into $\text{O}^+ + \text{D}$ (≤ 0.25 eV). This low KER_{OD} indicates that the process is most prominent near the dissociation threshold, and we only focus on these events in the following analysis.

Only two OD^+ states, namely $1^5\Sigma^-$ and $\text{B}^3\Sigma^-$, dissociate to ground-state $\text{O}^+(^4\text{S}) + \text{D}$ ^{39,40} (see Fig. 3). Our initial hypothesis was a subsequent SOC transition from the $a^1\Delta$ or $b^1\Sigma^+$ states of OD^+ to the $1^5\Sigma^-$ state (see Fig. 3), which then produces $\text{O}^+(^4\text{S}) + \text{D}$, i.e., generates the final products $\text{D}^+ + \text{O}^+ + \text{D}$. However, this scenario is very unlikely due to the higher KER_{OD} associated with this dissociation (see Fig. 3) and the required inefficient SOC transition between the singlet and quintet states (see Appendix E 2 for more details).

Spin-orbit mediated transitions from either the $a^1\Delta$ or the $b^1\Sigma^+$ states of OD^+ to the $\text{A}^3\Pi$ state, which we have shown to be a dominant route toward $\text{D}^+ + \text{O}(^3\text{P})$ dissociation,²¹ may lead to the $\text{O}^+(^4\text{S}) + \text{D}$ dissociation limit via additional transition(s). The $a^1\Delta$ or $b^1\Sigma^+$ to $\text{A}^3\Pi$ transitions are associated with a few tenths of picosecond lifetimes^{13,36} [corresponding to more than 100 vibrational periods of the relevant vibrational OD^+ ($a^1\Delta$, $b^1\Sigma^+$) states that are marked as black and green wavepackets in Fig. 3, which are on the order of a few femtoseconds]. Recently, Hechtfischer *et al.*³⁴ studied the photodissociation of OH^+ just above the $\text{H}^+ + \text{O}(^3\text{P})$ dissociation limit with high spectroscopic resolution. They noticed dissociation occurring predominantly in the $\text{H}^+ + \text{O}$ but also in the $\text{O}^+ + \text{H}$ final products. The observation of the latter channel was attributed to a non-adiabatic coupling of the $\text{A}^3\Pi$ state of OH^+ , correlated with the $\text{H}^+ + \text{O}(^3\text{P})$ dissociation limit, to states that are dissociating to the nearly degenerate $\text{O}^+(^4\text{S}) + \text{H}$ limit. That led us to consider the direct coupling of OD^+ ($\text{A}^3\Pi$) to either $1^5\Sigma^-$ or $\text{B}^3\Sigma^-$. After careful examination, we concluded that this direct coupling cannot produce a significant amount of $\text{O}^+ + \text{D}$ relative to the $\text{D}^+ + \text{O}$ yield (see Appendix E 2 for more details).

Another possibility is considering the ground $\text{X}^3\Sigma^-$ state as an additional OD^+ ($\text{X}^3\Sigma^-$) intermediate to facilitate the electron transfer. Both the $\text{A}^3\Pi$ and $\text{X}^3\Sigma^-$ states of OD^+ dissociate to $\text{D}^+ + \text{O}(^3\text{P})$; they are connected by a SOC, which, for intermediate to large R values, is, to a good approximation, just the fine-structure splitting of atomic oxygen and is R-independent. The $\text{X}^3\Sigma^-$ and $\text{B}^3\Sigma^-$ states, in turn, are more strongly coupled at large distances by electronic coupling than by the angular coupling that connects the $\text{A}^3\Pi$ and $\text{B}^3\Sigma^-$ states. O– D^+ charge-exchange between the X and $\text{B}^3\Sigma^-$ states has in fact been well-studied theoretically^{41–44} and experimentally,^{45,46} and the cross sections have been found to be significant near the threshold. Based on the calculations to be described below, we estimate the timescale of this $\text{A}^3\Pi \rightarrow \text{X}^3\Sigma^- \rightarrow \text{B}^3\Sigma^-$ dissociation sequence to be on the order of ≈ 700 ps.

In summary, we find that the most likely sequence of steps for sequential dissociation of D_2O^{2+} via the $\text{D}^+ + \text{OD}^+$ breakup, leading to $\text{O}^+(^4\text{S})$, involves the production of OD^+ ($a^1\Delta$, $b^1\Sigma^+$) intermediate ions from two-body dissociation on the 1^1B_1 and 2^1A_1 surfaces of the water dication, which then produce OD^+ ($\text{A}^3\Pi$) by SOC. An atomic spin-orbit interaction then strongly mixes the $\text{A}^3\Pi$ and $\text{X}^3\Sigma^-$ states, while an asymptotic electronic coupling between the $\text{X}^3\Sigma^-$ and $\text{B}^3\Sigma^-$ states triggers the charge-transfer that leads to the final reaction products $\text{D}^+ + \text{O}^+ + \text{D}$ [Scenario (2) in Appendix E 1]. The last step in this scenario is reminiscent of our earlier study of dissociative electron attachment to NH_3 molecules, where an asymptotic charge-transfer between $\text{NH}_2^- + \text{H}$ and $\text{H}^- + \text{NH}_2$ was

investigated.⁴⁷ Those states are split by 0.02 eV, just like the splitting in the present case of the OD⁺ dissociation, and we found in that case a transition probability of about 40%.

Competing Minor Dication State: Before proceeding with a quantitative examination of the efficiencies of the complex multi-step OD⁺(A³Π → X³Σ⁻ → B³Σ⁻) sequence of SOC and charge transfer transitions, we are now in a position to address the question raised above about the possibility of other dication states contributing to the O⁺ production at low-KER_{OD}. In particular, the 1³A₂ dication state, which lies energetically between the 1¹B₁ and 2¹A₁ states in the FC region, correlates directly with the intermediate OD⁺(A³Π) + D⁺ products. Since less than 1% of the 1³A₂ dication state decays via two-body breakup,¹³ it contributes predominantly via direct three-body fragmentation to the D⁺ + D⁺ + O production. Yet, the small percentage that does decay asymmetrically leads directly to OD⁺(A³Π) + D⁺, while the championed 1¹B₁ and 2¹A₁ states under study require a SOC to produce the A³Π state of OD⁺. Hence, further investigation with regard to this competing dissociation path is warranted. Figure 6 shows the electron sum energy that correlates with the production of D⁺ + O⁺ + D for low-KER_{OD} (≤0.25 eV). The distribution can be well fit using three states (employing only two states gave unsatisfactory fit results). The Gaussian width is extracted from the fit to the electron sum energy distribution for all events that result in the direct three-body channel D⁺ + D⁺ + O (not shown here). The difference between the widths of the 2¹A₁, 1³A₂, and 1¹B₁ dication states is very small (less than 10% disparity). Therefore, we used the same

widths for the fits of the three states. This procedure reveals that indeed the 1³A₂ dication state contributes around 24.2%. Since the SOC between the OD⁺(a¹Δ, b¹Σ⁺) and OD⁺(A³Π) cation states is the main cause for the sequential dissociation to be slow, removing that SOC will certainly make the breakup faster. Therefore, we can describe the breakup of D₂O²⁺(1³A₂) as a faster dissociation with little chance for at least one full revolution of the short-lived OD⁺(A³Π) transient, leading to OD⁺(A³Π)-D⁺ while populating continuum vibrational levels of OD⁺(A³Π) at or just above its dissociation limit in order to produce the low-KER_{OD}. The OD⁺(A³Π) transient cation state then connects to the OD⁺(X³Σ⁻) state by atomic SOC, followed by a charge-exchange to form OD⁺(B³Σ⁻), which then dissociates to O⁺ + D [Scenario (3) in Appendix E 1]. We will show elsewhere that the 1³A₂ dication state, which produces D⁺ + O⁺ + D exclusively by direct dissociation, affects events beyond the red rectangle in Fig. 4. It is the main contributor to the O⁺ production outside that rectangle, i.e., it produces D⁺ + O⁺ + D with a high-KER_{OD} (>0.25 eV). Nevertheless, the analysis of the slow sequential decay of the 1¹B₁ and 2¹A₁ dication states suffers from some contamination caused by the fast-sequential breakup of the 1³A₂ state, which we estimate to be 17% and 38%, respectively. These contributions are also causing the skewness observed in Fig. 5. They stem from the different angular distribution of the contributions outside the red rectangle in Fig. 4.

C. Dissociation branching ratios of transient electronically excited OD⁺

Theoretical Treatment: In the present context, we concluded that the X³Σ⁻ state of the OD⁺ intermediate facilitates the transfer from the A³Π to the B³Σ⁻ state of the transient ionic fragment. To test this hypothesis, we carried out a simplified time-dependent treatment of the OD⁺ dissociation dynamics initiated in the A³Π state. The formalism employed for this half-collision problem is analogous to the one used to study dissociative electron attachment.⁴⁸ The calculations were initiated by placing a vibrational wavefunction from either the a¹Δ or the b¹Σ⁺ state on the A³Π PEC of OD⁺. We chose vibrational levels with J = 0 at or above the A³Π dissociation limit (e.g., ν = 11 for a¹Δ and ν = 7 for b¹Σ⁺). We then solved the three-channel time-dependent Schrödinger equation, coupling the A³Π, X³Σ⁻, and B³Σ⁻ states, employing a constant SOC between the A and X states and electronic coupling between the X and B³Σ⁻ states, the latter taken from Ref. 41. From the half Fourier transform of the wavepackets on the three PECs evaluated at the dissociation limit, we obtained the final populations of the three electronic states and, hence, the O⁺ + D and D⁺ + O branching ratios as a function of KER_{OD}, bearing in mind that the X and A states both dissociate to the same [D⁺ + O(³P)] limit.

For initial vibrational wavepackets from either the a¹Δ or b¹Σ⁺ excited states of OD⁺, placed on the A³Π PEC, we find that the O⁺ + D and D⁺ + O branching ratios decrease as a function of KER_{OD} from threshold. For example, starting with the vibrational levels ν = 12 and 13 of the a¹Δ state, with corresponding KERs of 0.12 and 0.30 eV (ignoring the 0.02 eV energy difference between the D⁺ + O and O⁺ + D dissociation limits), the corresponding branching ratios are 0.023 and 0.018, respectively. We hasten to point out that this simplified treatment, in addition to ignoring the small asymptotic energy difference between the B and the A and X

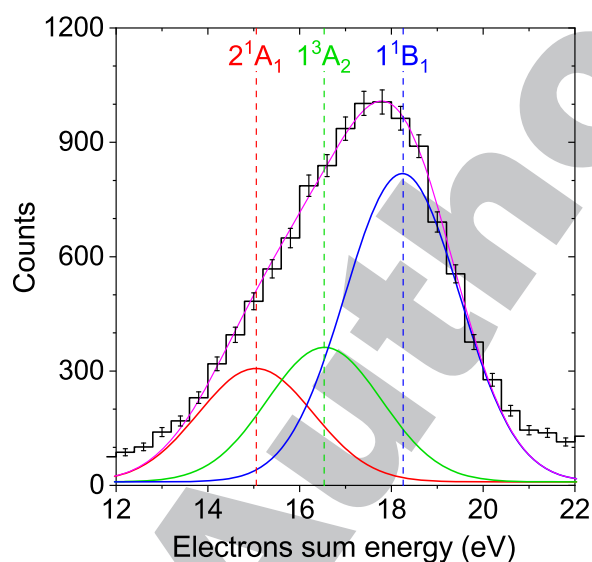


FIG. 6. Measured electron sum energy, E_{esum} , for the dication states leading to low-KER_{OD} (≤0.25 eV) contributions of the D⁺ + O⁺ + D fragmentation channel (black line) upon PDI of D₂O with 61 eV photons. The vertical lines indicate the positions of the dication states. Three Gaussians are fitted to the data. The first Gaussian fit (red line) represents the 2¹A₁ dication state (20.4 ± 1%), the second Gaussian fit (green line) represents the 1³A₂ dication state (24.2 ± 1.2%), the third Gaussian fit (blue line) represents the 1¹B₁ dication state (55.4 ± 0.9%), and the sum of all three Gaussians is shown as the magenta line. All error bars reflect one standard deviation of the statistical uncertainty.

dissociation limits in carrying out the time propagations, also ignores the effects of fine-structure splittings between the $O(^3P)$ states^{34,41,44} as well as rotational effects, all of which can be significant near threshold. For the vibrational level $\nu = 11$ of the $a^1\Delta$ state, which fortuitously lies very close to the $D^+ + O$ dissociation limit (see Fig. 3), we took the non-degeneracy of the $D^+ + O$ and $O^+ + D$ dissociation limits into account when choosing the energy differences between the initial vibrational level and the final asymptotic limits. As a result, the computed branching ratio for the $\nu = 11$ vibrational level of the $a^1\Delta$ state is 0.105. Unfortunately, in the case of the $b^1\Sigma^+$ state, there is no vibrational level close to the $D^+ + O$ dissociation limit, so the simplified model does not allow us to provide a threshold branching ratio for the $b^1\Sigma^+$ state. We shall see below that, despite the simplifications made, the dependence of the calculated branching ratios, BRs, on the KER_{OD} is in reasonable qualitative agreement with the experiment.

Branching Ratios of OD^+ Dissociations: On the experimental side, we turn again to the native frames analysis of the measured data, with which we are able to investigate the sequential breakup of D_2O^{2+} in great detail. We note that the dissociation via the two states of the OD^+ intermediate, $a^1\Delta$ and $b^1\Sigma^+$, can be separated in the experiment by the slanted line in the KER correlation map shown in Fig. 7(a) for the $D^+ + D^+ + O$ channel,²¹ which only represents the events from the sequential breakup. This KER correlation map shows this reaction channel's PDI yield as a function of the KER of the first step, $KER_{OD,D}$, and the KER of the second step, KER_{OD} . The ratios of the yields of these two fragmentation pathways, originating from the $D_2O^{2+}(1^1B_1, 2^1A_1)$ dications and leading to the $a^1\Delta$ and $b^1\Sigma^+$ states of the OD^+ intermediate, are around 37% and 63%, respectively, as extracted from the counts left and right of the slanted line in Fig. 7(a). In Fig. 7(b), we show a similar KER correlation map for the breakup generating the $D^+ + O^+ + D$ final products. The events with $KER_{OD} \leq 0.25$ eV (below the red dashed line) mainly represent the sequential dissociation processes in this reaction channel (compare to Fig. 4). With this identification, we can now compare the sequential breakup scenarios that are active in the $D^+ + D^+ + O$ channel [Fig. 7(a)] with the scenarios in the $D^+ + O^+ + D$ channel [Fig. 7(b)]. One can clearly see that in the latter case, the

transition via the $OD^+(a^1\Delta)$ state dominates the O^+ production at low KER_{OD} .

The fact that both final products of the OD^+ predissociation, namely $D^+ + O$ and $O^+ + D$, are measured simultaneously in their respective reaction channels, $D^+ + D^+ + O$ and $D^+ + O^+ + D$, allows us to compare their transition probabilities and, with this, the probability for an additional transition leading to $O^+ + D$ instead of $D^+ + O$. This comparison is made as a function of the energy above the dissociation limits within the common $KER_{OD} \leq 0.25$ eV window [note: we neglect the small energy difference between the $D^+ + O(^3P)$ and $O^+(^4S) + D$ dissociation limits shown in Fig. 3]. This is accomplished by computing the BRs for the $D^+ + O^+ + D$ channels, given by

$$BR(a^1\Delta, b^1\Sigma^+) = \frac{N(D^+ + O^+ + D)}{N(D^+ + O^+ + D) + N(D^+ + D^+ + O)}, \quad (6)$$

where the measured yields N are for the specific intermediate OD^+ states $a^1\Delta$ and $b^1\Sigma^+$. In order to remove the effect of the experimental resolution on the measured KER_{OD} distribution, we have used the simulated KER_{OD} (see Appendix C for details) for the calculation of the state-selective BRs in both reaction channels. We account for the possible systematic uncertainties in the measured branching ratios as follows: We note that we lose less than 0.5% of the $D^+ + D^+$ counts due to the multi-hit dead-time response of the detector for the $D^+ + D^+ + O$ channel, which for some events requires measuring two D^+ ions with similar time-of-flight that hit the detector at neighboring positions. Moreover, the counts of the $D^+ + O^+ + D$ reaction channel are corrected for the imperfect gate isolating the direct PDI from the autoionization mechanism, which has been achieved by monitoring the electron energy sharing (not shown here). Additionally, the pollution in the $D^+ + O^+ + D$ channel from the direct three-body fragmentation of the 1^1B_1 state, as discussed in Sec. III A, and from the fast-sequential breakup of the $D_2O^{2+}(1^3A_2)$ dication state, as discussed in Sec. III B, has been accounted for. After all these corrections, we estimate the remaining experimental relative uncertainty of the extracted BRs to be less than 10%, which has been added to the respective statistical errors.

In Fig. 8, we show the BRs, representing the probabilities to produce $D^+ + O^+ + D$ from the $a^1\Delta$ and $b^1\Sigma^+$ states of the excited OD^+ intermediate with respect to the sum of both sequential breakup channels, namely $D^+ + O^+ + D$ and $D^+ + D^+ + O$ [see Eq. (6)]. The BRs are a function of energy above the dissociation limit KER_{OD} , which is truncated for both the $D^+ + O^+ + D$ and $D^+ + D^+ + O$ channels at $KER_{OD} \leq 0.25$ eV. Since both the $a^1\Delta$ and $b^1\Sigma^+$ states of OD^+ dissociate via a SOC mediated transition to the $A^3\Pi$ state, which leads to the $D^+ + O(^3P)$ products, a sequence of additional transitions is needed to yield the observed $O^+(^4S) + D$ fragments. Assuming that the transition probabilities are products of the probabilities of each transition along the path, which means the transitions are independent from each other, the branching ratio is a measure of the $A^3\Pi \rightarrow X^3\Sigma^- \rightarrow B^3\Sigma^-$ transition sequence probability to produce the measured $O^+ + D$ reaction products (denoted hereafter as P_{A-X-B}). Quantitatively, $P_{A-X-B} = BR$ if $BR \ll 1$, otherwise, $P_{A-X-B} = BR/(1-BR)$. Moreover, as this BR is independent of the transition leading to the $OD^+(A^3\Pi)$ state, one can expect the BRs of the $a^1\Delta$ and $b^1\Sigma^+$ states of OD^+ as a function of KER_{OD} above the dissociation limit to be the same. Within the error bars, the observed

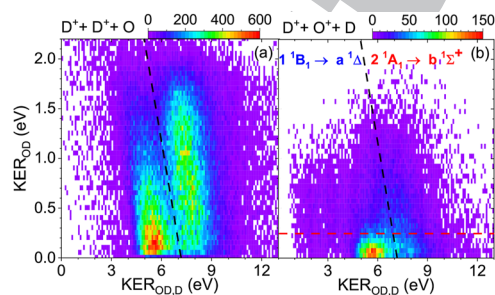
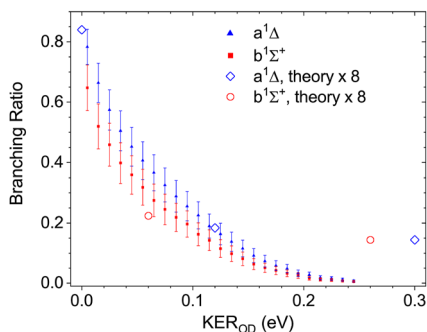


FIG. 7. KER correlation maps for the sequential fragmentation of $D_2O^{2+}(1^1B_1, 2^1A_1)$ after PDI of D_2O at 61 eV via $D^+ + OD^+$ followed by the dissociation of the intermediate molecular ion (a) $OD^+ \rightarrow D^+ + O$ (i.e., $D^+ + D^+ + O$ final products) (adapted from Ref. 21), and (b) $OD^+ \rightarrow O^+ + D$ (i.e., $D^+ + O^+ + D$ final products). The dashed lines separate the two states $a^1\Delta$ and $b^1\Sigma^+$ of the transient OD^+ at $KER_{OD,D} + KER_{OD} = 7.18$ eV.



678 **FIG. 8.** The $D^+ + O^+ + D$ branching ratios with respect to the combined
679 $D^+ + O^+ + D$ and $D^+ + D^+ + O$ production upon sequential dissociation of
680 D_2O^{2+} ($1^1B_1, 2^1A_1$) according to Eq. (6) for the $OD^+(a^1\Delta)$ state (blue solid tri-
681 angles and open diamonds) and the $OD^+(b^1\Sigma^+)$ state (red solid squares and open
682 circles), separated in Fig. 7, for the same KER_{OD} range (≤ 0.25 eV).

683 near-congruence of the two measured BRs presented in Fig. 8
684 (solid blue triangles and red squares) confirms the interpretation
above.

685 While the trends of the calculated BRs as a function of KER_{OD}
686 are in reasonable agreement with the experiment, the theoretical BRs
687 are roughly 8 times smaller than the experimental results, which
688 is not very surprising given the somewhat coarse model employed
689 here, as described above. However, in the case of the $a^1\Delta$ state,
690 the theory results qualitatively confirm the experimental findings
691 reasonably well. Figure 8 shows that for $KER_{OD} \leq 0.04$ eV, the likelihood
692 of producing the reaction products $D^+ + O^+ + D$ is higher than the
693 likelihood of generating $D^+ + D^+ + O$. This very low KER of OD^+
694 corresponds to a very slow dissociation and provides more time for
695 efficient SOC, which is needed in this complex multi-step sequential
696 dissociation process.

697 Finally, we note that our calculations with $J = 0$ were conducted
698 for very few vibrational states, i.e., the ones within the relevant
699 energy window. In contrast, the experiment smoothly spans the
700 whole energy range because of the wide angular momentum distribu-
701 tion of the OD^+ intermediate.²¹ The explicit angular momentum
702 (J) dependence of these multi-step transitions calls for further
703 theoretical work.

704 IV. CONCLUSION AND SUMMARY

705 We identified two specific pathways in the rare dissociation
706 of D_2O^{2+} into $D^+ + O^+ + D$. Both are initiated by populating
707 either the 1^1B_1 or the 2^1A_1 electronic dication states by direct PDI,
708 dissociating initially into $D^+ + OD^+$ intermediates. Applying our
709 highly differential measurements and analysis methods in combina-
710 tion with coupled-channel time-dependent dynamics calculations,
711 we have investigated state-selectively the possible sequential frag-
712 mentation mechanisms of the D_2O^{2+} dication, proceeding through
713 the formation of excited OD^+ transients to feed the rare $D^+ + O^+$
714 $+ D$ three-body breakup channel following PDI of water with a single
715 61 eV photon (see Fig. 1).

716 The first step of the dissociation pathway eventually leading to
717 $D^+ + O^+ + D$, namely the breakup into $D^+ + OD^+$, is similar to our
718 previous observation of the more prominent $D^+ + D^+ + O$ reaction

channel.²¹ The second step, specifically the predissociation of the
 $a^1\Delta$ and $b^1\Sigma^+$ states of the OD^+ transient ion, requires SOC to pro-
duce $OD^+(A^3\Pi)$, which starts dissociating toward the $D^+ + O(^3P)$
limit. However, to then generate the very rare reaction $D^+ + O^+$
 $+ D$ channel under investigation here, the subsequent pathway,
diverting a small fraction of the events on the potential energy
landscape toward the $D^+ + O^+ + D$ breakup, is more involved. It
turns out that an additional atomic SOC connects the $OD^+(A^3\Pi)$
state to the $OD^+(X^3\Sigma^-)$ state, and the latter transient ion under-
goes an asymptotic charge-transfer through electronic coupling to
the $OD^+(B^3\Sigma^-)$ state, which eventually dissociates into $O^+(^4S) +$
 D , as these states are nearly degenerate for O–D distances greater
than 6 bohrs. Apparently, this complex multi-step $A^3\Pi \rightarrow X^3\Sigma^-$
 $\rightarrow B^3\Sigma^-$ sequence of SOC and charge transfer transitions domi-
nates over competing single transition paths like $A^3\Pi \rightarrow B^3\Sigma^-$ at
low- KER_{OD} . An analogous electron transfer at similar interme-
diate distances (≈ 18 bohrs), without the need for SOC and hence of
greater efficiency, has been observed recently in the PDI of NH_3 .⁴⁹

Evidently, upon PDI of heavy water creating D_2O^{2+} , SOC effec-
tively changes the course of the $D^+ + D^+ + O$ dissociation process
toward the $D^+ + O^+ + D$ fragmentation channel by triggering charge
redistribution and electron transfer in the sequential photodissocia-
tion route via OD^+ transients as a function of the KER (see Fig. 1).
The key to the direct measurement of the $A^3\Pi \rightarrow X^3\Sigma^- \rightarrow B^3\Sigma^-$
transition probability in the transient OD^+ ion in our experiments
is the simultaneous measurement of both sequential fragmentation
channels, i.e., $D^+ + O^+ + D$ and $D^+ + D^+ + O$, combined with the
fact that both dissociation paths have a common first step, namely
the SOC transition to the intermediate $OD^+(A^3\Pi)$ fragment ion.
The BR of the transient OD^+ ion to dissociate into $O^+(^4S) + D$
instead of $D^+ + O(^3P)$ varies with its KER and is similar for both
 $a^1\Delta$ and $b^1\Sigma^+$ states of the OD^+ intermediate. Apparently, feeding
the $D^+ + O^+ + D$ reaction channel quickly becomes inefficient with
increasing KER_{OD} of the dissociating OD^+ intermediate, as there
is less time for effective SOC and the BRs drop to zero. On the other
hand, under certain circumstances, the transient OD^+ ion dissoci-
ates more efficiently to $O^+ + D$ than $D^+ + O$. This can be seen in
Fig. 8 for double ionization events where the kinetic energy release
of the transient KER_{OD} is lower than 0.04 eV. For these very slow
dissociation processes of $OD^+(a^1\Delta, b^1\Sigma^+)$, the branching ratios for
producing $D^+ + O^+ + D$ exceed 0.5, i.e., they contribute more than
the $D^+ + D^+ + O$ breakups.

705 ACKNOWLEDGMENTS

706 We acknowledge T. Weinacht for sparking our interest in this
707 scarce water fragmentation channel. Work at LBNL was supported
708 by the U.S. Department of Energy (DOE), Office of Science, Basic
709 Energy Sciences (BES), under Award No. DE-AC02-05CH11231.
710 This research used resources from the Advanced Light Source (ALS)
711 and the National Energy Research Scientific Computing Center
712 (NERSC), both DOE Office of Science User Facilities under Contract
713 No. DE-AC02-05CH11231. In particular, we acknowledge NERSC
714 Award Nos. BES-ERCAP-0020143 (theory) and BES-ERCAP-
715 0019776 (experiment). We acknowledge the staff of the ALS, in
716 particular beamline 10.0.1, for their outstanding support. The
717 JRM personnel were supported by the U.S. Department of Energy
718

774 (DOE), Office of Science, Basic Energy Sciences (BES), under Award
775 No. DE-FG02-86ER13491. UNR personnel acknowledge support
776 from the National Science Foundation under Award Nos. NSF-
777 1807017 and NSF-2208017. We are indebted to the RoentDek Com-
778 pany for long-term support with detector software and hardware.

779 AUTHOR DECLARATIONS

780 Conflict of Interest

781 The authors have no conflicts to disclose.

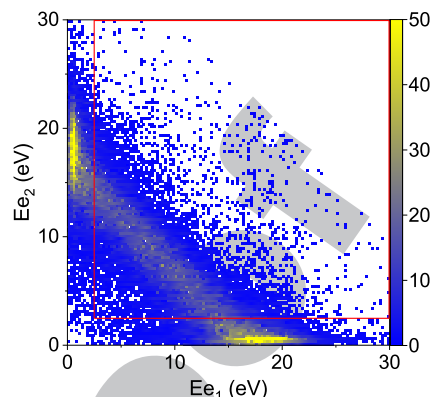
782 Author Contributions

783 W.I. and Th.W. designed the experiment. W.I., Th.W., K.A.L.,
784 B.G., J.B.W., B.J., D.C., V.D., T.S., and D.S.S. conducted the
785 beam time and acquired the experimental data at the Advanced
786 Light Source. W.I. and T.S. analyzed the data. T.N.R., A.E.O.,
787 and Z.L.S. performed the calculations. W.I., T.N.R., I.B.-I., and
788 Th.W. wrote the manuscript with significant review and editing
789 by T.S., D.S.S., C.W.M., and R.R.L., which all co-authors
790 approved. W.I., T.S., I.B.-I., T.N.R., C.W.M., and Th.W. created the
791 figures.

792 **W. Iskandar:** Conceptualization (equal); Formal analysis (lead);
793 Investigation (equal); Visualization (lead); Writing – original draft
794 (lead); Writing – review & editing (equal). **T. N. Rescigno:** For-
795 mal analysis (equal); Investigation (equal); Visualization (equal);
796 Writing – original draft (equal); Writing – review & editing
797 (equal). **A. E. Orel:** Formal analysis (equal); Investigation (equal);
798 Writing – review & editing (equal). **T. Severt:** Formal analy-
799 sis (equal); Investigation (equal); Visualization (equal); Writing –
800 review & editing (equal). **K. A. Larsen:** Investigation (equal);
801 Writing – review & editing (supporting). **Z. L. Streeter:** Invest-
802 igation (supporting); Writing – review & editing (supporting).
803 **B. Jochim:** Investigation (supporting). **B. Griffin:** Invest-
804 igation (supporting). **D. Call:** Investigation (supporting). **V. Davis:** Invest-
805 igation (supporting); Writing – review & editing (supporting). **C.**
806 **W. McCurdy:** Funding acquisition (equal); Investigation (support-
807 ing); Writing – review & editing (equal). **R. R. Lucchese:** Funding
808 acquisition (equal); Investigation (supporting); Writing – review &
809 editing (supporting). **J. B. Williams:** Investigation (supporting).
810 **I. Ben-Itzhak:** Funding acquisition (equal); Investigation (equal);
811 Supervision (equal); Visualization (supporting); Writing – original
812 draft (equal); Writing – review & editing (equal). **D. S. Slaughter:**
813 Conceptualization (supporting); Funding acquisition (equal);
814 Investigation (equal); Project administration (equal); Supervision
815 (equal); Writing – review & editing (lead). **Th. Weber:** Con-
816 ceptualization (lead); Data curation (lead); Funding acquisition
817 (lead); Investigation (lead); Project administration (lead); Supervi-
818 sion (equal); Writing – original draft (equal); Writing – review &
819 editing (equal).

820 DATA AVAILABILITY

821 The data that support the findings of this study are available
822 from the corresponding author upon reasonable request.

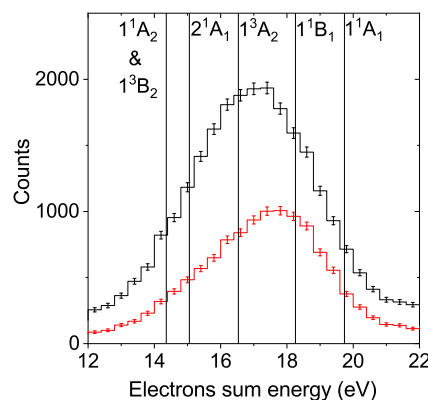


823 **FIG. 9.** Electron energy correlation map for all photo double ionization events lead-
824 ing to the $D^+ + O^+ + D$ fragmentation channel at 61 eV. The contributions from
825 autoionization have been excluded by gating on the events in the red rectangle.

826 APPENDIX A: WATER DICATION STATES

827 The electron-electron energy correlation map for all photo dou-
828 ble ionization events leading to the $D^+ + O^+ + D$ fragmentation
829 channel at 61 eV is shown in Fig. 9. In the remainder of the analysis,
830 the autoionization channel is excluded by taking only the events in
831 the red rectangle into account.

832 By plotting the measured sum energy of both detected elec-
833 trons, we can identify which water dication states have been popu-
834 lated in the direct double ionization (DDI). The vertical lines in
835 Fig. 10 indicate the positions of the dication states at the equi-
836 librium geometry of the neutral water molecule derived from the
837 potential energy curves in Ref. 20. Note that the calculations of
838 Streeter *et al.* in Ref. 20 incorrectly place the $H^+ + H^+ + O$ asymp-
839 tote 0.2 eV above the $H^+ + O^+ + H$ limit. This error is related to
840 the difficulty of calculating the ionization potential (IP) of atomic
841 oxygen (13.618 eV) relative to that of hydrogen (13.598 eV) and



842 **FIG. 10.** Electron sum energy, $E_{e_{sum}}$, for the direct double ionization (DDI) process
843 leading to the $D^+ + O^+ + D$ fragmentation channel. All error bars reflect one
844 standard deviation of the statistical uncertainty. Black lines and symbols: all KER_{OD}
845 contributions. Red lines and symbols: for $0 \leq KER_{OD} \leq 0.25$ eV.

846 **TABLE I.** Electronic states of water dications and their electronic configurations in C_{2v} symmetry, the two- and three-body dissociation products, and thermochemical thresholds
847 for the generated products. The electronic configuration of neutral water is given as $1a_1^2 2a_1^2 1b_2^2 3a_1^2 1b_1^2$.

| C_{2v} sym. | Electronic configuration | 2-Body dissoci. limit | 3-Body dissoci. limit | Thermochemical threshold (eV) |
|---------------|----------------------------------|---------------------------|-----------------------|-------------------------------|
| 851 X^3B_1 | $(3a_1 1b_1)^{-1}$ | $OD^+(X^3\Sigma^-) + D^+$ | $D^+ + D^+ + O(^3P)$ | 36.86 |
| 852 1^1A_1 | $(1b_1)^{-2}$ | $OD^+(a^1\Delta) + D^+$ | $D^+ + D^+ + O(^1D)$ | 38.83 |
| 853 1^1B_1 | $(3a_1 1b_1)^{-1}$ | $OD^+(a^1\Delta) + D^+$ | $D^+ + D^+ + O(^1D)$ | 38.83 |
| 854 1^3A_2 | $(1b_2 1b_1)^{-1}$ | $OD^+(A^3\Pi) + D^+$ | $D^+ + D^+ + O(^3P)$ | 36.86 |
| 855 2^1A_1 | $(3a_1)^{-2}$ | $OD^+(b^1\Sigma^+) + D^+$ | $D^+ + D^+ + O(^1D)$ | 38.83 |
| 856 1^1A_2 | $(1b_2 1b_1)^{-1}$ | $OD^+(^1\Pi) + D^+$ | $D^+ + D^+ + O(^1D)$ | 38.83 |
| 857 1^3B_2 | $(1b_2 3a_1)^{-1}$ | $OD^+(A^3\Pi) + D^+$ | $D^+ + D^+ + O(^3P)$ | 36.86 |
| 858 2^3A_2 | $(1b_2 1b_1 3a_1)^{-1} 4a_1^1$ | $OD^+(B^3\Sigma^-) + D^+$ | $D^+ + D + O(^4S)$ | 36.88 |
| 859 2^3B_1 | $(3a_1)^{-2} (1b_1)^{-1} 4a_1^1$ | $OD^+(B^3\Sigma^-) + D^+$ | $D^+ + D + O(^4S)$ | 36.88 |

861 has been taken into account here. The black line and symbols rep-
862 resent the electron sum energy distribution for DDI events (no
863 restriction on KER_{OD}), while the red line and symbols show the
864 events with $KER_{OD} \leq 2.5$ eV, which stem from mostly the sequen-
865 tial breakup of the OD^+ intermediate into $O^+ + D$ (see also Fig. 6
866 and related text for further analysis). The electronic configurations
867 (in C_{2v} geometry), the two-body and three-body dissociation lim-
868 its of the states, as well as the thermochemical thresholds are given
in Table I.

869 APPENDIX B: NATIVE FRAMES ANALYSIS METHOD

870 The native frames analysis method is based on the use of the
871 conjugate momenta of the Jacobi coordinates, which describe the
872 relative positions of the three fragments.^{21,37,38} For D_2O fragmenting
873 into $D^+ + O^+ + D$ via the intermediate $D^+ + OD^+$, the conjugated
874 momentum associated with the first breakup step is given by

$$875 \mathbf{P}_{OD_{II},D_I} = \frac{m_{OD}}{M} \mathbf{P}_{D_I} - \frac{m_D}{M} [\mathbf{P}_{D_{II}} + \mathbf{P}_O], \quad (B1)$$

876 where \mathbf{P}_{D_I} and \mathbf{P}_O are the measured momenta of the D^+ and O^+
877 fragments, respectively, while $\mathbf{P}_{D_{II}}$ is the momentum of the neutral
878 D fragment evaluated from momentum conservation. (Note that in
879 the equations, we denote the D^+ and D fragments as D_I and D_{II} ,
880 respectively.) In this case, m_D is the mass of D^+ , m_{OD} is the mass of
881 OD^+ , and M is the mass of the D_2O^{2+} dication.

882 Similarly, the conjugate momentum associated with the second
883 breakup step is

$$884 \mathbf{P}_{OD_{II}} = \mu_{OD} \left[\frac{\mathbf{P}_{D_{II}}}{m_D} - \frac{\mathbf{P}_O}{m_O} \right], \quad (B2)$$

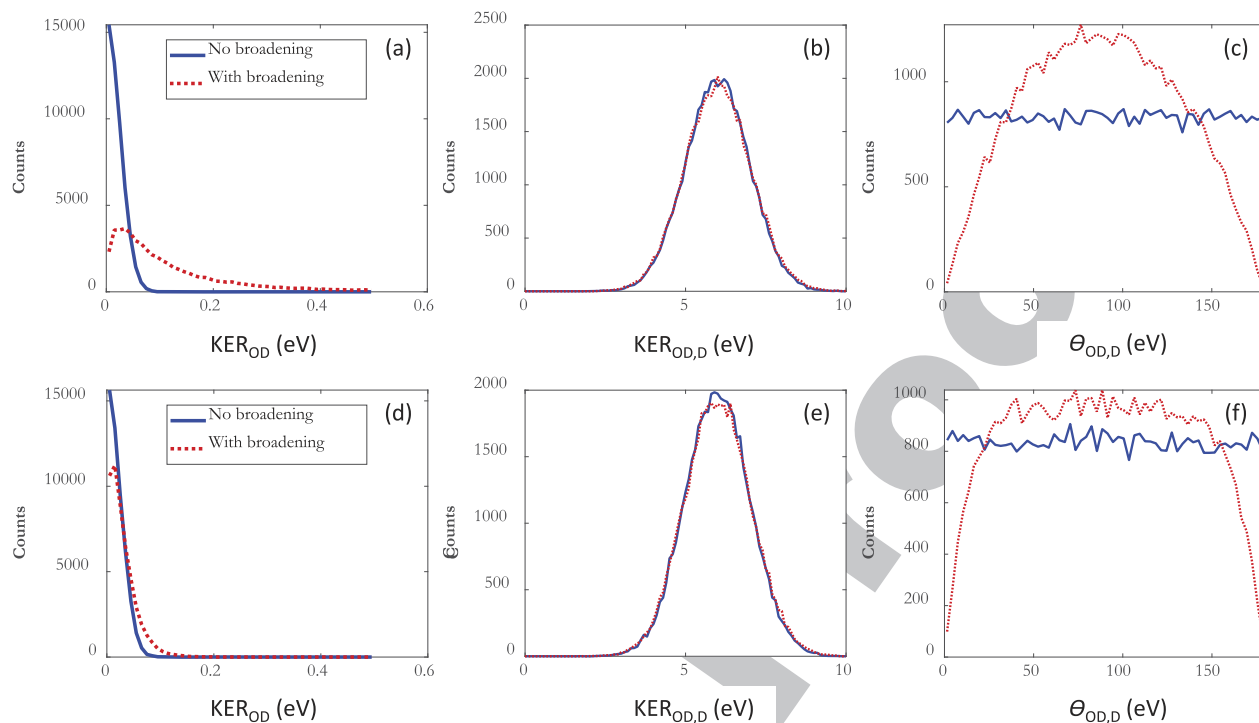
885 where μ_{OD} is the reduced mass of OD^+ . The angle between these
886 two vectors, θ_{OD_{II},D_I} , is evaluated from the scalar product of the con-
887 jugate momenta given in Eqs. (B1) and (B2). Finally, the KERs of
888 the first and second steps are given by $KER_{OD_{II},D_I} = \mathbf{P}_{OD_{II},D_I}^2 / 2\mu_{OD,D}$
889 (where $\mu_{OD,D}$ is the reduced mass of $D^+ - OD^+$) and $KER_{OD_{II}}$
890 = $\mathbf{P}_{OD_{II}}^2 / 2\mu_{OD}$, respectively.

891 APPENDIX C: MONTE-CARLO SIMULATION

892 We perform a Monte-Carlo simulation to determine the
893 impact of the experimental uncertainties on the measured dis-
894 tribution of the angle between the conjugate momenta given in
895 Eqs. (B1) and (B2), $N(\theta_{OD,D})$, i.e., the direction of the assumed
896 two breakup steps, as well as the KER in the second step. As
897 this KER_{OD} approaches zero, it becomes harder to define the
898 angle $\theta_{OD,D}$, and this effect is also addressed by this simula-
899 tion. Specifically, we assume that the distribution is uniform, i.e.,
900 $N(\theta_{OD,D}) = \text{constant}$, and simulate how it becomes distorted due
901 to the finite experimental resolution. To achieve this, we first
902 compute the momenta of the three fragments upon dissociation
903 using the measured KER associated with each step of the sequen-
904 tial breakup and span $\theta_{OD,D}$ randomly over the whole angular
905 range.

906 The angular and energy resolution of the detected fragment
907 ions are affected by (a) the size of the interaction volume defined
908 by the overlap between the synchrotron light and gas jet beam (≈ 1.0
909 $\times 0.3 \times 0.3$ mm³), (b) the temperature of the supersonic gas tar-
910 get (≈ 50 K parallel and ≈ 15 K perpendicular to the jet propagation
911 direction), and (c) the time (≈ 0.5 ns) and position (≈ 0.25 mm)
912 uncertainties of our particle detectors.

913 We generate a random distribution of the initial positions of
914 the D_2O molecules to match the interaction volume defined by the
915 crossing of the molecular jet and synchrotron beam, given explic-
916 itly by the boundary condition (a). To satisfy condition (b), we
917 generate a center-of-mass (CM) velocity distribution for the D_2O
918 molecules in the supersonic jet of our COLTRIMS setup. Next, using
919 this “initial” CM-velocity and the point of origin of each fragment,
920 combined with the $N(\theta_{OD,D}) = \text{constant}$ distribution, we compute
921 its impact time and position on the detector by solving the equa-
922 tions of motion in our COLTRIMS spectrometer. Then, we add
923 the uncertainty due to the detector resolution, given in point (c)
924 above, to the simulated impact data. Using the resulting dataset,
925 we compute the momenta of the D^+ and O^+ fragments for each
926 event (i.e., single molecule) by applying the same algorithm as for
927 the measured data. Likewise, the momentum of the neutral D frag-
928 ment is computed using momentum conservation. The resulting
929 simulated momenta now include the main experimental uncertain-
930 ties listed in the experimental broadening conditions (a)–(c) above.



931 **FIG. 11.** Simulations of the relevant observables of the native frames analysis of the $D^+ + O^+ + D$ (a)–(c) and $D^+ + D^+ + O$ (d)–(f) fragmentation channels with (red dashed
932 curve) and without (solid blue curve) experimental broadening (see text) show the uncertainties effect on the KER_{OD} (a), (d), $KER_{OD,D}$ (b), (e), and $\theta_{OD,D}$ (c), (f) distributions.

959
960

933 This process is repeated for about the same number of events as in
934 the measured dataset to achieve similar statistical quality as in the
935 experiment.

936 The simulation, which includes the experimental resolutions
937 and yields a non-uniform distribution that is similar to the
938 measured spread, indicates significant distortion of the expected
939 $N(\theta_{OD,D}) = \text{const.}$ angular distribution, as shown in Fig. 5. The near
940 congruence of the observed and simulated distributions suggests
941 that the measured $\theta_{OD,D}$ spread represents what one should expect
942 for a uniform angular distribution in $\theta_{OD,D}$ of a sequential fragmen-
943 tation via an intermediate transient molecule, i.e., OD^+ rotating in
944 the fragmentation plane, under the influence of the uncertainties
945 of our experiment [for comparison, see the uniform distribution in
946 Fig. 2(c) in Ref. 21 for the $D^+ + D^+ + O$ channel]. This notable
947 distortion of the angular distribution is rooted in the momentum
948 of the detected O^+ ion, which is on the order of the D^+ momen-
949 tum but results in low kinetic energy of this heavy fragment and,
950 hence, little excursions on the ion detector and a small spread in
951 time-of-flight.

952 The KER_{OD} distribution of the second fragmentation step is
953 also affected by the experimental resolutions, becoming broader
954 than it should be. This broadening was corrected for the BR data
955 shown in Fig. 8.

956 In contrast to the large distortions in the $D^+ + O^+ + D$
957 channel, the same simulation for the $D^+ + D^+ + O$ fragmen-
958 tation channel, measured simultaneously, i.e., affected by the same

961 experimental uncertainties, demonstrates that distortions of the
962 reported uniform angular distribution, $N(\theta_{OD,D})$, and the second
963 breakup step KER_{OD} distribution [see Fig. 2(c) in Ref. 21] are sig-
964 nificantly smaller. This difference between the $D^+ + D^+ + O$ and the
965 $D^+ + O^+ + D$ channels is due to the much better momentum res-
966 olution of the detected D^+ ions as compared to the O^+ ions in our
967 measurements.

968 To visualize this distortion, we show in Fig. 11 how the simu-
969 lated uncertainties affect the relevant observables of the native
970 frames analysis while assuming the same KER_{OD} and $KER_{OD,D}$
971 distributions for both fragmentation channels. We find that, while the
972 KER_{OD} distribution broadens in panel (a), the assumed flat (uni-
973 form) $\theta_{OD,D}$ angular distribution for the $D^+ + O^+ + D$ channel in
974 panel (c) becomes peaked at around 90° . We see no effect of the
975 simulated uncertainties on the $KER_{OD,D}$ distribution in panel (b)
976 for the $D^+ + O^+ + D$ fragmentation. In contrast to the $D^+ + O^+$
977 $+ D$ fragmentation, the broadening of the KER_{OD} distribution in
978 the $D^+ + D^+ + O$ reaction channel is barely noticeable in panel
979 (d). The assumed flat (uniform) $\theta_{OD,D}$ angular distribution remains
980 flat in most parts but develops dips for very small and large angles
981 of the $D^+ + D^+ + O$ fragmentation in panel (f). In summary, the
982 same experimental uncertainties result in significantly smaller dis-
983 tortions of the expected flat (uniform) angular distribution $\theta_{OD,D}$
984 between the conjugate momenta of the two fragmentation steps and
985 the KER_{OD} of the second dissociation step in the latter reaction
986 channel.

961
962
963
964
965
966
967
968
969
970
971
972
973
974
975
976
977
978
979
980
981
982
983
984
985
986

APPENDIX D: EXPERIMENTAL SHIFTS AND BROADENING—IMPACT OF THE EXPERIMENTAL RESOLUTION ON THE RELATIVE ANGLES OF THE FRAGMENTS

For the discussion of the kinematics of the considered dissociation routes, the angular resolutions of the fragments have to be taken into account. In the lab frame, the average momentum uncertainty of O^+ ions is approximately ± 1.9 a.u., while the uncertainty for the D^+ ion is about ± 0.7 a.u. The derived momentum of the neutral D fragment is low and peaks around 5.8 a.u. It has a significant momentum uncertainty of about ± 2.3 a.u., which has a large impact on the corresponding angular distribution. While integrating over the direction of the polarization vector, we define the molecular breakup frame via the measured momenta of the three heavy fragments in the laboratory frame, which establish a plane (similar to a Newton plot). The azimuthal relative angles $\phi_{A,B}$ between the fragments A and B are measured around the normal of this plane [$\arctan(p_A/p_B)$] and shown in Fig. 12. The uncertainties of the relative angles between D^+ and D and between O^+ and D are on average $\pm 31^\circ$ and $\pm 33^\circ$, respectively, while the uncertainty of the relative angle between O^+ and D^+ ions is notably better (about $\pm 3^\circ$).

A deconvolution, comprising the finite momentum resolution of the measured fragment pair angles ϕ_{O^+,D^+} , which peak at 175° in Fig. 12, yields sharp distributions shifted to 180° (not shown here). The deconvoluted $\phi_{D^+,D}$ and $\phi_{O^+,D}$ angular distributions peak at 180° and 0° , respectively, but are notably broader. These observed large shifts in the measured relative angles $\phi_{D^+,D}$ and $\phi_{O^+,D}$ in Fig. 12 are to be expected for particles that fly in the opposite or the same direction when the uncertainty of the center-of-mass-momentum of this subsystem is on the order of one of their momentum vectors. This is because the finite resolution in these emission scenarios provides ample phase space to redistribute yield away from a strict parallel or anti-parallel orientation of the momentum vectors, which are scarce combinations to begin with due to the small solid angle. The situation is different for relative angles larger than 0° and smaller than 180° because the solid angle, and, hence, the yield

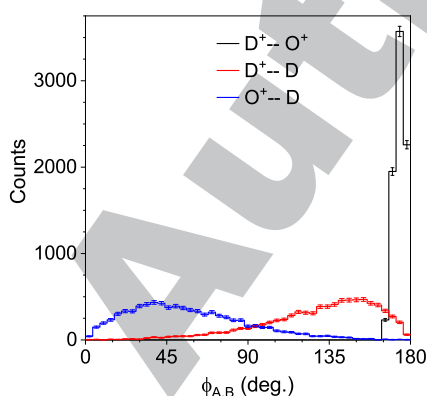


FIG. 12. Relative angles $\phi_{A,B}$ in the molecular breakup plane of D_2O^{2+} between fragment pairs D^+ and O^+ (black), D^+ and D (red), and O^+ and D (blue) for the $KER_{OD} \leq 0.25$ eV feature, marked as the red rectangle in Fig. 4. All error bars represent one standard deviation of statistical uncertainty.

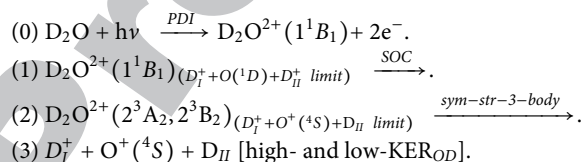
for these orientations of the momentum vectors, is much larger. Consequently, the finite lab frame angular resolutions mentioned above will mainly result in a broadening of the relative angles but little to no shift for the measured relative angles of fragment pairs approaching 90° that are contributing to the events inside the red rectangle and beyond in Fig. 4.

APPENDIX E: CONSIDERED DISSOCIATION MECHANISMS OF THE 1^1B_1 , 2^1A_1 , AND 1^3A_2 WATER DICATION STATES

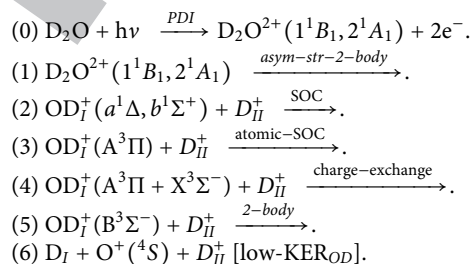
1. Overview of fragmentation scenarios

The D fragments, which are subject to electron transfer, are distinguished by as D_{II} , while D_I represents the D^+ ions that remain unaffected.

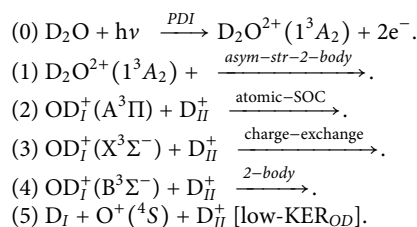
SCENARIO (1): Direct Fragmentation



SCENARIO (2): Slow Sequential Fragmentation



SCENARIO (3): Fast Sequential Fragmentation



2. Alternative less likely dissociation routes of the $OD^+(a^1\Delta, b^1\Sigma^+)$ intermediate in Scenario (2)

The dissociation of the $OD^+(a^1\Delta, b^1\Sigma^+)$ intermediate into $O^+ + D$ to yield $D^+ + O^+(^4S) + D$ in the measurement could take place in several ways. Bearing in mind that only two OD^+ states, namely $1^5\Sigma^-$ and $B^3\Sigma^-$, dissociate to ground-state $O^+(^4S) + D$ ^{39,40} (see Fig. 3), and assuming either $D_2O^{2+}(1^1B_1$ or $2^1A_1)$ dications to dissociate into $D^+ + OD^+(a^1\Delta$ or $b^1\Sigma^+)$ in the first step, our initial hypothesis was a subsequent SOC transition from the $a^1\Delta$ or $b^1\Sigma^+$ states of OD^+ to the $5^5\Sigma^-$ state (see Fig. 3), which then produces $O^+(^4S) + D$, i.e., generates the final products $D^+ + O^+ + D$. Considering the lowest PECs of the OD^+ intermediate ion, shown in Fig. 3, we then expect a direct predissociation from the $a^1\Delta$ and $b^1\Sigma^+$

states to the final $1^5\Sigma^-$ state, mediated by SOC, to be strongest near the crossings between these PECs. The KERs associated with these crossings are expected to peak around 0.31 and 0.67 eV, respectively (see Fig. 3), while the measured KER associated with this dissociation step is much lower, specifically peaking around 0.06 eV. This reason, along with the fact that SOC between singlet and quintet states is quite small, leads us to conclude that these pathways are clearly not the dominant ones.

As a direct transition of the $\text{OD}^+(\text{a}^1\Delta, \text{b}^1\Sigma^+)$ to the $1^5\Sigma^-$ state seems unlikely, we then took into account that a transition to the $\text{OD}^+(\text{A}^3\Pi)$ takes place first. Yet, spin-orbit mediated transitions from either the $\text{a}^1\Delta$ or the $\text{b}^1\Sigma^+$ states of OD^+ to the $\text{A}^3\Pi$ state, which we have shown to be a dominant route toward $\text{D}^+ + \text{O}(\text{P})$ dissociation,²¹ may lead to the $\text{O}^+(\text{S}) + \text{D}$ dissociation limit by several pathways. One possibility is an additional spin-orbit transition between the $\text{A}^3\Pi$ and the final $1^5\Sigma^-$ states along the dissociation path. This can be viewed as a third step along this sequence of fragmentation steps, which starts with D_2O^{2+} breaking up to $\text{D}^+ + \text{OD}^+$, followed by the predissociation of the OD^+ intermediate via the $\text{A}^3\Pi$ state toward the $\text{D}^+ + \text{O}(\text{P})$ limit, and ends with $\text{A}^3\Pi \rightarrow 1^5\Sigma^-$, i.e., a spin-orbit mediated transition that leads to the $\text{O}^+(\text{S}) + \text{D}$ dissociation limit of interest in this work. Hechtfisher *et al.*,³⁴ however, pointed out that the $\text{A}^3\Pi$ and $1^5\Sigma^-$ states only interact through second-order SOC, which they, therefore, did not consider in their detailed modeling of near-threshold photodissociation of OH^+ .

Instead of this second SOC mediated path, which is very unlikely to take place as the states involved in the transitions have different symmetry as well as spin, an electron transfer in the fragmenting OD^+ intermediate between the $\text{A}^3\Pi$ state, dissociating into $\text{D}^+ + \text{O}(\text{P})$, and the $\text{B}^3\Sigma^-$ state, dissociating into the measured $\text{O}^+(\text{S}) + \text{D}$, appears more probable. These states run parallel, separated by ≈ 0.02 eV, for O–D distances greater than 6 bohrs toward their respective limits, as seen in Fig. 3, and, hence, provide ample time for the charge transfer. A non-adiabatic transition between the Π and Σ states is facilitated by a matrix element describing the electronic orbital angular momentum coupling, as laid out by Wolniewicz *et al.*⁵⁰ The matrix element falls off as $1/R^2$. We modified our structure codes to include this property and found that at ≈ 6 bohrs, the coupling matrix element is ≈ 0.025 a.u. However, since this angular coupling derives from the nuclear kinetic energy, it enters the Hamiltonian with a factor of one over the reduced mass ($1/\mu_{\text{OD}} = 1/3264$ a.u.) and is hence very small. Wavepacket calculations confirmed that this angular coupling resulted in a negligible transfer of population to the $\text{O}^+(\text{S}) + \text{D}$ channel. As the likelihoods for the above contemplated dissociation routes appear to be very small, we were left with considering a complex multi-step $\text{OD}^+(\text{a}^1\Delta \text{ or } \text{b}^1\Sigma^+ \rightarrow \text{A}^3\Pi \rightarrow \text{X}^3\Sigma^- \rightarrow \text{B}^3\Sigma^-)$ sequence of SOC and charge transfer transitions as described in the main text (see Sec. III B).

3. Direct breakup of $\text{D}_2\text{O}^+(\text{1}^1\text{B}_1, \text{2}^1\text{A}_1)$ into $\text{D}^+ + \text{O}^+ + \text{D}$ for Scenario (1)

In the following, we describe why a second dissociation scenario for the 1^1B_1 water dication state, i.e., the direct fragmentation into $\text{D}^+ + \text{O}^+ + \text{D}$ via the intermediate $\text{D}^+ + \text{D}^+ + \text{O}$ three-body breakup step [Scenario (1) in Appendix E 1], needs to be considered

a small contribution, according to our measurement and theoretical description. We begin with the latter.

Out of the three water dication state candidates 2^1A_1 , 1^3A_2 , and 1^1B_1 , only the last state is seen to have a shallow well in symmetric C_{2v} geometry, which supports efficient SOC (see Fig. 13); the other states are purely repulsive. However, a vertical transition from the equilibrium geometry of neutral water produces the 1^1B_1 dication roughly 1 eV above the symmetric barrier near 4.5 bohrs. Furthermore, the isolated crossing between the 1^1B_1 and the 2^3A_2 dication states near 5.5 bohrs is unlikely to result in a charge exchange. Nevertheless, since the 1^1B_1 PEC is steeply repulsive near the equilibrium geometry of neutral water, non-vertical transitions within the FC region can produce dications at or below the aforementioned symmetric barrier that trap dications in the shallow 1^1B_1 potential well and thus increase the probability of a spin-orbit induced charge exchange with the 2^3A_2 state, which we estimate to take over 100 oscillations and, hence, more than 100 femtoseconds. To model this process, we carried out classical trajectory calculations on the 1^1B_1 surface, as was performed in Ref. 20. The idea was to estimate the fraction of the trajectories that pass between the top of the 1^1B_1 barrier at 5.1 eV and the point where the 1^1B_1 and 2^3A_2 surfaces cross, which is 0.25 eV lower, establishing a small appearance window in the potential energy landscape (see Fig. 13 as well as Ref. 49 for a similar appearance window in NH_3).

While sampling from a Wigner distribution of initial states, we selected only those trajectories with a total energy less than 5.1 eV (correlated with the top of the barrier) and having one deuteron with an energy less than 0.25 eV, approximating $\text{KER}_{\text{OD}} \leq 0.25$ eV. Of the 100 000 trajectories sampled leading to the three-body breakup, roughly 0.3% met these criteria, i.e., this small amount of trajectories passes through the narrow energy appearance window where trapping is possible. However, not all such trapped dications must necessarily undergo charge transfer via SOC.

We also found that the accepted trajectories always tend to open the DOD angle, which is also consistent with our finding that,

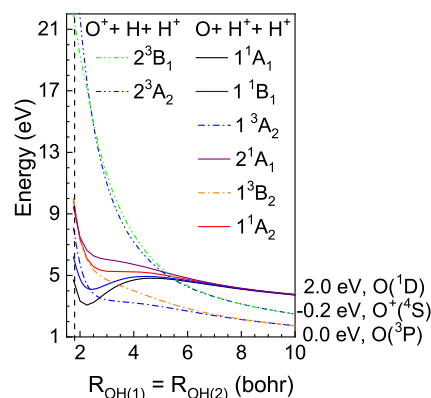


FIG. 13. PECs for the symmetric breakup of the H_2O^{2+} states dissociating into $\text{H}^+ + \text{H}^+ + \text{O}$ and $\text{H}^+ + \text{O}^+ + \text{H}$; adapted from Ref. 20 and corrected by -0.77 eV. The zero energy value of the y-axis corresponds to the $\text{H}^+ + \text{H}^+ + \text{O}(\text{P})$ dissociation limit with a PDI threshold of 36.7 eV.³ The photon energy of 61 eV, hence, corresponds to 24.3 eV on the ordinate.

near the geometry of neutral water, the energy of the 1^1B_1 dication state is lowered with increasing HOH bond angle, i.e., the dissociation angle $\phi_{D^+,D}$ is expected to be bigger than the bond angle of neutral D_2O (104.5°). The small amount of trajectories means that only up to 16% of the 1^1B_1 state contributions in the red rectangle of Fig. 4 fragment in a direct way; the remaining events dissociate sequentially as described in the paper.

We complement the theoretical interpretation with our experimental observations. This is discussed in the lab frame and molecular frame while taking the momentum and angular resolution of the fragments (discussed in Appendix D) into account. The momentum correlation maps of the three heavy fragments in the lab frame are shown in Fig. 14 for the events that reside inside the red rectangle in Fig. 4 and which are associated with the 2^1A_1 , 1^3A_2 , and 1^1B_1 water dication states. Figure 14 reveals that the momentum of the neutral D fragment is ≈ 6 times lower than that of the D^+ ion.

Given this momentum balance, a contribution to the $D^+ + O^+ + D$ fragmentation having low KER_{OD} can be conceivably facilitated via the intermediate $D^+ + D^+ + O$ three-body breakup step [see Fig. 13 and Scenario (1) in Appendix E 1]. We conclude this from the aforementioned non-vertical transitions within the FC region leading to the top of the 1^1B_1 barrier and populating the 2^3A_2 dication surface 0.25 eV below via SOC after a symmetric O–D stretch. During this fragmentation step, the energy of this appearance window is released and mostly distributed equally among the light D^+ ions. Accordingly, both fragments yielded about ≈ 0.125 eV at the crossing (corresponding to a momentum of ≈ 5.8 a.u.), while the oxygen fragment received almost no kinetic energy (≈ 0.025 eV) in this first dissociation step. After the electron transfer, the neutralized D^+ ion is expected to receive no additional energy, which corresponds to the measured momentum of 5.8 a.u. we observe. On the other hand, the O^+ fragment will receive most of its kinetic energy in the subsequent dissociation step between itself and the other D^+ fragment ion. These two ions repel each other due to the Coulomb explosion, and the O^+ ion is emitted in the direction of the neutralized D fragment (we discuss the relative angles in more detail below). Accordingly,

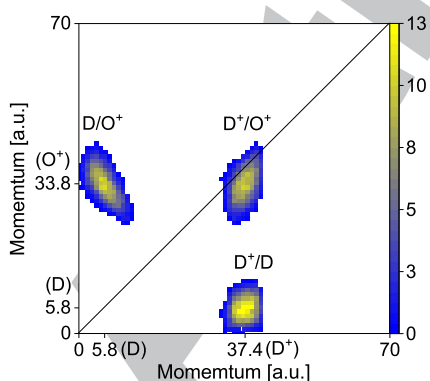


FIG. 14. Lab frame fragment momentum-correlation diagram: yield attributed to the 1^1A_1 and 1^1B_1 dication states of water after PDI at 61 eV resulting in $D^+ + O^+ + D$ for the low KER_{OD} feature, marked as the red rectangle in Fig. 4, as a function of the momenta of the fragment pairs D^+ , O^+ , and D : see labels at axes and islands.

the kinetic energy release KER_{OD} between the O fragment and the to-be-neutralized D^+ ion yields low values that partly reside inside the red rectangle of Fig. 4. After this SOC and state crossing, the 2^3A_2 and 2^3B_1 PECs will lead to the detected final products $D^+ + O^+ (^4S) + D$.

Throughout the remaining discussion, we mark the D-fragment subject to electron transfer as D_{II} and the unchanged D^+ ion as D_I^+ for this direct three-body breakup.

After the second step of the dissociation happens and the electron is transferred from the neutral oxygen atom to the deuteron, the neutralized D_{II} fragment no longer experiences a Coulomb repulsion from the other ionic D_I^+ fragment. Instead, the now charged O^+ fragment is repelled by the D_I^+ ion in the third step. Accordingly, the D_I^+ ion is expected to have higher momentum than the O^+ ion, which is corroborated in Fig. 14 (the feature lying just under the diagonal). Furthermore, we expect to see a momentum correlation between the O^+ ion and the neutralized D fragment, reflecting where, or in other words, how early or late, SOC on the PECs is taking place, as apparent in Fig. 14. The low momentum of the neutral D fragment and the high momentum of the O^+ ion tell us that the crossing is happening shortly after the direct PDI took place. The crossing would happen later if the momentum of the neutral D_{II} fragment was high and the momentum of the O^+ ion was low. Our momentum map agrees with the former scenario. The momentum map also shows a clear correlation between the neutral D_{II} fragment and the O^+ ion in the sense that the deuteron has less momentum when the O^+ ion exhibits more momentum and vice versa (see the -1 slope of the D/O^+ island in Fig. 14, i.e., the upper left feature). This reflects that the large momentum of the fast D_I^+ fragment is imparted on the $O + D^+$ center of the mass system. Opposite the fast D_I^+ ion, the neutral O fragment appears to follow the slow D_{II} ion, while the latter two particles do not repel each other.

Using the momentum of the neutralized D_{II} fragment in Fig. 14, we can estimate the time between the first and second dissociation steps. Before it is neutralized, the D_{II}^+ ion travels from the FC region at around 1.8 a.u. to the crossing between the 1^1B_1 and 2^3A_2 water dication states at around 5.5 bohrs with a momentum of circa 5.8 a.u. Classically, the time can be estimated at ~ 56 fs.

We support and quantify our findings in momentum space with the analysis of the relative dissociation angles between the measured D_I^+ and O^+ ions and the deduced neutral D_{II} fragment. The relative angle between the O^+ ion and the deuteron presented in Fig. 12 peaked at 40° (blue line). Apparently, both particles were preferentially emitted with a small relative angle, which is necessary for an effective electron transfer between the two fragments in the intermediate step of the dissociation process and which yields low- $KER_{OD_{II}}$. Moreover, we can identify a near back-to-back emission of the O^+ and D_I^+ ions with a relative emission angle peaking at 175° (black line). We also see that the D_I^+ ion and the neutral D_{II} fragment are emitted with a large relative angle, which peaks at 148° (red line) to a degree that is similar to the width of the relative angular distribution between the neutral D_{II} fragment and the O^+ ion. This again points to a larger bond angle of the water dication. A Walsh diagram of the 1^1B_1 dication state of water with an electron in the $4a_1$ orbital shows that, indeed, the bond opening is slightly preferred in the FC region.^{13,20} In summary, the direct three-body fragmentation

1269 scenario [Scenario (1) in Appendix E 1] requires an almost linear
1270 water dication in order to produce the $D_1^+ + O^+ + D_{II}$ reaction
1271 products. A large relative emission angle between the two D^+ ions
1272 was also observed for the direct fragmentation of the 1^1B_1 dication
1273 state into $D^+ + D^+ + O$.¹⁴

1274 REFERENCES

- 1275 ¹D. Fedorov, S. Koseki, M. W. Schmidt, and M. S. Gordon, "Spin-orbit coupling in
1276 molecules: Chemistry beyond the adiabatic approximation," *Int. Rev. Phys. Chem.*
1277 **22**, 551 (2003).
1278 ²C. Marian, "Spin-orbit coupling and intersystem crossing in molecules," *Wiley*
1279 *Interdiscip. Rev.: Comput. Mol. Sci.* **2**, 187 (2012).
1280 ³P. J. Richardson, J. H. D. Eland, P. G. Fournier, and D. L. Cooper, "Spectrum and
1281 decay of the doubly charged water ion," *J. Chem. Phys.* **84**, 3189 (1986).
1282 ⁴D. Winkoun, G. Dujardin, L. Hellner, and M. J. Besnard, "One- and two-step
1283 double photoionisation processes in valence shells of H_2O ," *J. Phys. B: At., Mol.*
1284 *Opt. Phys.* **21**, 1385 (1988).
1285 ⁵M. N. Piancastelli, A. Hempelmann, F. Heiser, O. Gessner, A. Rüdél, and
1286 U. Becker, "Resonant photofragmentation of water at the oxygen K edge by
1287 high-resolution ion-yield spectroscopy," *Phys. Rev. A* **59**, 300 (1999).
1288 ⁶J. Laksman, E. P. Månsson, A. Sankari, D. Céolin, M. Gisselbrecht, and S. L.
1289 Sorensen, "Rapid bond rearrangement in core-excited molecular water," *Phys.*
1290 *Chem. Chem. Phys.* **15**, 19322 (2013).
1291 ⁷G. H. Olivera, C. Caraby, P. Jardin, A. Cassimi, L. Adoui, and B. Gervais,
1292 "Multiple ionization in the earlier stages of water radiolysis," *Phys. Med. Biol.* **43**,
1293 2347 (1998).
1294 ⁸F. Alvarado, R. Hoekstra, and T. Schlathöler, "Dissociation of water molecules
1295 upon keV H^+ - and He^{9+} - induced ionization," *J. Phys. B: At., Mol. Opt. Phys.*
1296 **38**, 4085 (2005).
1297 ⁹S. W. J. Scully, J. A. Wyer, V. Senthil, M. B. Shah, and E. C. Montene-
1298 gro, "Autodissociation of doubly charged water molecules," *Phys. Rev. A* **73**,
1299 040701(R) (2006).
1300 ¹⁰E. C. Montenegro, S. W. J. Scully, J. A. Wyer, V. Senthil, and M. B. Shah,
1301 "Evaporation, fission and auto-dissociation of doubly charged water," *J. Electron*
1302 *Spectrosc. Relat. Phenom.* **155**, 81 (2007).
1303 ¹¹S. J. King and S. D. Price, "Electron ionization of H_2O ," *Int. J. Mass Spectrom.*
1304 **277**, 84 (2008).
1305 ¹²R. Singh, P. Bhatt, N. Yadav, and R. Shanker, "Kinematics and dissociation
1306 dynamics of a water molecule under the impact of 10 keV electrons," *J. Phys. B:*
1307 *At., Mol. Opt. Phys.* **46**, 085203 (2013).
1308 ¹³B. Gervais, E. Giglio, L. Adoui, A. Cassimi, D. Duflo, and M. E. Galassi, "The
1309 H_2O^{2+} potential energy surfaces dissociating into H^+/OH^+ : Theoretical analysis
1310 of the isotopic effect," *J. Chem. Phys.* **131**, 024302 (2009).
1311 ¹⁴D. Reedy, J. B. Williams, B. Gaire, A. Gattón, M. Weller, A. Menssen, T. Bauer,
1312 K. Henrichs, P. Burzynski, B. Berry, Z. L. Streeter, J. Sartor, I. Ben-Itzhak, T.
1313 Jahnke, R. Dörner, T. Weber, and A. L. Landers, "Dissociation dynamics of the
1314 water dication following one-photon double ionization. II. Experiment," *Phys.*
1315 *Rev. A* **98**, 053430 (2018).
1316 ¹⁵H. C. Straub, B. G. Lindsay, K. A. Smith, and R. F. Stebbings, "Absolute partial
1317 cross sections for electron-impact ionization of H_2O and D_2O from threshold to
1318 1000 eV," *J. Chem. Phys.* **108**, 109 (1998).
1319 ¹⁶A. Hiraya, K. Nobusada, M. Simon, K. Okada, T. Tokushima, Y. Senba,
1320 H. Yoshida, K. Kamimori, H. Okumura, Y. Shimizu, A.-L. Thomas, P. Mil-
1321 lie, I. Koyano, and K. Ueda, " H_2^+ formation from H_2O^+ mediated by the
1322 core-excitation-induced nuclear motion in H_2O ," *Phys. Rev. A* **63**, 042705 (2001).
1323 ¹⁷I. Ben-Itzhak, A. M. Sayler, M. Leonard, J. W. Maseberg, D. Hathiramani, E.
1324 Wells, M. A. Smith, J. Xia, P. Wang, K. D. Carnes, and B. D. Esry, "Bond rear-
1325 rangement caused by sudden single and multiple ionization of water molecules,"
1326 *Nucl. Instrum. Methods Phys. Res., Sect. B* **233**, 284 (2005).
1327 ¹⁸F. A. Rajgara, A. K. Dharmadhikari, D. Mathur, and C. P. Safvan, "Strong fields
1328 induce ultrafast rearrangement of H atoms in H_2O ," *J. Chem. Phys.* **130**, 231104
(2009).

- 1329 ¹⁹M. Leonard, A. M. Sayler, K. D. Carnes, E. M. Kaufman, E. Wells, R. Cabrera-
1330 Trujillo, B. D. Esry, and I. Ben-Itzhak, "Bond rearrangement during Coulomb
1331 explosion of water molecules," *Phys. Rev. A* **99**, 012704 (2019).
1332 ²⁰Z. L. Streeter, F. L. Yip, R. R. Lucchese, B. Gervais, T. N. Rescigno, and
1333 C. W. McCurdy, "Dissociation dynamics of the water dication following
1334 one-photon double ionization. I. Theory," *Phys. Rev. A* **98**, 053429 (2018).
1335 ²¹T. Severt, Z. L. Streeter, W. Iskandar, K. A. Larsen, A. Gattón, D. Trabert,
1336 B. Jochim, B. Griffin, E. G. Champenois, M. M. Brister, D. Reedy, D. Call,
1337 R. Strom, A. L. Landers, R. Dörner, J. B. Williams, D. S. Slaughter, R. R. Lucchese,
1338 Th. Weber, C. W. McCurdy, and I. Ben-Itzhak, "Step-by-step state-selective track-
1339 ing of fragmentation dynamics of water dications by momentum imaging," *Nat.*
1340 *Commun.* **13**, 5146 (2022).
1341 ²²J. Rajput and C. P. Safvan, "Fragmentation of water by ion impact: Kinetic
1342 energy release spectra," *Phys. Rev. A* **84**, 052704 (2011).
1343 ²³K. H. Tan, C. E. Brion, P. E. Van der Leeuw, and M. J. van der Wiel, "Absolute
1344 oscillator strengths (10–60 eV) for the photoabsorption, photoionisation and
1345 fragmentation of H_2O ," *Chem. Phys.* **29**, 299 (1978).
1346 ²⁴J. H. D. Eland, "Double photoionisation spectra of methane, ammonia and
1347 water," *Chem. Phys.* **323**, 391 (2006).
1348 ²⁵Interesting alternatives to the approach presented here are multiple-spawning
1349 surface dynamics and non-adiabatic *ab initio* molecular dynamics (AIMD) meth-
1350 ods, where electronic energies, gradients, and non-adiabatic coupling matrix
1351 elements (NACMEs) are computed on-the-fly [see, e.g., B. F. E. Curchod and T.
1352 J. Martinez, *Chem. Rev.* **118**, 3305 (2018), and K. Gope *et al.*, *J. Phys. Chem.*
1353 *Lett.* **11**, 8108 (2020)]. For smaller molecules such as water, non-adiabatic AIMD
1354 treatments are very much feasible with the presently available computational tools.
1355 ²⁶W. Iskandar, T. N. Rescigno, A. E. Orel, K. A. Larsen, B. Griffin, D. Call,
1356 V. Davis, B. Jochim, T. Severt, J. B. Williams, I. Ben-Itzhak, D. S. Slaughter, and Th.
1357 Weber, "Atomic autoionization in the photo-dissociation of super-excited deuter-
1358 ated water molecules fragmenting into $D^+ + O^+ + D$," *Phys. Chem. Chem. Phys.*
1359 **25**, 21562 (2023).
1360 ²⁷Z. Ali, Y.-D. Chuang, D. Kilcoyne, A. Aguilar, S.-K. Mo, and Z. Hussain,
1361 "Upgrade of the beamline 10.0.1 at the advanced light source," *Proc. SPIE* **8502**,
1362 85020P (2012).
1363 ²⁸R. Dörner, V. Mergel, O. Jagutzki, L. Spielberger, J. Ullrich, R. Moshhammer,
1364 and H. Schmidt-Böcking, "Cold target recoil ion momentum spectroscopy: A
1365 'momentum microscope' to view atomic collision dynamics," *Phys. Rep.* **330**, 95
(2000).
1366 ²⁹J. Ullrich, R. Moshhammer, A. Dorn, R. Dörner, L. P. H. Schmidt, and H.
1367 Schmidt-Böcking, "Recoil-ion and electron momentum spectroscopy: Reaction-
1368 microscopes," *Rep. Prog. Phys.* **66**, 1463 (2003).
1369 ³⁰T. Jahnke, T. Weber, T. Osipov, A. Landers, O. Jagutzki, L. P. H. Schmidt, C. L.
1370 Cocke, M. H. Prior, H. Schmidt-Böcking, and R. Dörner, "Multicoincidence stud-
1371 ies of photo and auger electrons from fixed-in-space molecules using the coltrims
1372 technique," *J. Electron Spectrosc. Relat. Phenom.* **141**, 229 (2004).
1373 ³¹R. Dörner, T. Weber, M. Achler, V. Mergel, L. Spielberger, O. Jagutzki, F.
1374 Afaneh, C. L. Cocke, and H. Schmidt-Böcking, "3-D coincident imaging spec-
1375 troscopy for ions and electrons," in *Imaging in Chemical Dynamics* (Oxford
1376 University Press, 2000), Chap. 20, pp. 339–349.
1377 ³²O. Jagutzki, A. Cerezo, A. Czasch, R. Dörner, M. Hattas, M. Huang, V. Mergel,
1378 U. Spillmann, K. Ullmann-Pfleger, T. Weber, H. Schmidt-Böcking, and G. Smith,
1379 "Multiple hit readout of a microchannel plate detector with a three-layer delay-line
1380 anode," *IEEE Trans. Nucl. Sci.* **49**, 2477 (2002).
1381 ³³M. Krems, J. Zirbel, M. Thomason, and R. D. DuBois, "Channel electron mul-
1382 tiplier and channelplate efficiencies for detecting positive ions," *Rev. Sci. Instrum.*
1383 **76**, 093305 (2005).
1384 ³⁴U. Hechtfisher, J. Levin, M. Lange, L. Knoll, D. Schwalm, R. Wester, A. Wolf,
1385 and D. Zajfman, "Near-threshold photodissociation of cool OH^+ to $O + H^+$ and
1386 $O^+ + H$," *J. Chem. Phys.* **151**, 044303 (2019).
1387 ³⁵J. E. Sansonetti and W. C. Martin, "Handbook of basic atomic spectroscopic
1388 data," *J. Phys. Chem. Ref. Data* **34**, 1559 (2005).
1389 ³⁶R. de Vivie, C. M. Marian, and S. D. Peyerimhoff, "Spin-forbidden transitions
1390 in the presence of an intersystem crossing: Application to the $b^1\Sigma^+$ state in OH^+ ,"
1391 *Chem. Phys.* **112**, 349 (1987).
1392 ³⁷J. Rajput, T. Severt, B. Berry, B. Jochim, P. Feizollah, B. Kaderiya, M. Zohrabi,
1393 U. Ablikim, F. Ziaee, P. Kanaka Raju, D. Rolles, A. Rudenko, K. D. Carnes,

- 1394 B. D. Esry, and I. Ben-Itzhak, "Native frames: Disentangling sequential from
1395 concerted three-body fragmentation," *Phys. Rev. Lett.* **120**, 103001 (2018).
- 1396 ³⁸T. Severt, "Imaging light-induced molecular fragmentation dynamics," Ph.D.
1397 thesis, Kansas State University, 2021.
- 1398 ³⁹D. M. Hirst and M. F. Guest, "An *ab initio* study of the excited states of OH⁺,"
1399 *Mol. Phys.* **49**, 1461 (1983).
- 1400 ⁴⁰D. R. Yarkony, "Spin-forbidden predissociation of the rovibronic levels of
1401 OH⁺(c¹Π)," *J. Phys. Chem.* **97**, 111 (1993).
- 1402 ⁴¹G. Chambaud, B. Levy, J. M. Launay, P. Millie, E. Roueff, and F. T. Minh,
1403 "Charge exchange and fine-structure excitation in O-H⁺ collisions," *J. Phys. B:
1404 At. Mol. Phys.* **13**, 4205 (1980).
- 1405 ⁴²P. C. Stancil, D. R. Schultz, M. Kimura, J.-P. Gu, G. Hirsch, and R. J. Buenker,
1406 "Charge transfer in collisions of O⁺ with H and H⁺ with O," *Astron. Astrophys.,
1407 Suppl. Ser.* **140**, 225 (1999).
- 1408 ⁴³J. A. Spirko, J. T. Mallis, and A. P. Hickman, "Calculation of adiabatic and
1409 diabatic ³Σ⁻ states of OH⁺," *J. Phys. B: At., Mol. Opt. Phys.* **33**, 2395 (2000).
- 1410 ⁴⁴J. A. Spirko, J. J. Zirbel, and A. P. Hickman, "Quantum mechanical scattering
1411 calculations for charge exchange: O + H⁺ ↔ O⁺ + H," *J. Phys. B: At., Mol. Opt.
1412 Phys.* **36**, 1645 (2003).
- ⁴⁵F. C. Fehsenfeld and E. E. Ferguson, "Thermal energy reaction rate constants
for H⁺ and CO⁺ with O and NO," *J. Chem. Phys.* **56**, 3066 (1972). 1413 1414
- ⁴⁶W. Federer, H. Villinger, F. Howorka, W. Lindinger, P. Tosi, D. Bassi, and
E. Ferguson, "Reaction of O⁺, CO⁺, and CH⁺ ions with atomic hydrogen," *Phys.
Rev. Lett.* **52**, 2084 (1984). 1415 1416 1417
- ⁴⁷T. N. Rescigno, C. S. Trevisan, A. E. Orel, D. S. Slaughter, H. Adaniya,
A. Belkacem, M. Weyland, A. Dorn, and C. W. McCurdy, "Dynamics of
dissociative electron attachment to ammonia," *Phys. Rev. A* **93**, 052704
(2016). 1418 1419 1420
- ⁴⁸P. L. Gertitschke and W. Domcke, "Time-dependent wave-packet description
of dissociative electron attachment," *Phys. Rev. A* **47**, 1031 (1993). 1421 1422
- ⁴⁹K. A. Larsen, T. N. Rescigno, T. Severt, Z. L. Streeter, W. Iskandar, S.
Heck, A. Gattton, E. G. Champenois, R. Ström, B. Jochim, D. Reedy, D. Call,
R. Moshhammer, R. Dörner, A. L. Landers, J. B. Williams, C. W. McCurdy,
R. R. Lucchese, I. Ben-Itzhak, D. S. Slaughter, and T. Weber, "Photoelectron
and fragmentation dynamics of the H⁺ + H⁺ dissociative channel in NH₃
following direct single-photon double ionization," *Phys. Rev. Res.* **2**, 043056
(2020). 1423 1424 1425 1426 1427 1428
- ⁵⁰L. Wolniewicz, T. Orlikowski, and G. Staszewska, "¹Σ_u and ¹Π_u states of
the hydrogen molecule: Nonadiabatic couplings and vibrational levels," *J. Mol.
Spectrosc.* **238**, 118 (2006). 1429 1430 1431